NUMERICAL AND EXPERIMENTAL STUDY OF BEHAVIOUR OF REINFORCED MASONRY COLUMNS

by

Seyed Alireza Siadat

Submitted in partial fulfilment of the requirements

for the degree of Master of Applied Science

at

Dalhousie University

Halifax, Nova Scotia

November 2023

I dedicate this dissertation to my family

for their endless love, support, and encouragement.

Table of Contents

List of Tables

List of Figures

Abstract

This study investigated the behaviour of reinforced concrete (RC) masonry columns with an emphasis on assessing the moment magnifier method specified in the Canadian masonry design standard CSA S304-14 for design of masonry columns. As the CSA S304-14 provisions on masonry column design simply adopted those for masonry wall design, their applicability to masonry columns have not been thoroughly studied either experimentally or numerically. In this research, six RC masonry columns of several influential design parameters were tested under concentric and eccentric axial loads until failure. Additionally, 20 archetype models were developed using the finite element method in SAP2000 to further assess the validity of CSA S304-14 provisions for columns of a wide range of slenderness. The American masonry design standard and TMS 402/602 was also used to provide another source for comparison between the experimental and FE model results and available code values.

The experimental results revealed that the failure modes of specimens were dependent on their slenderness and loading conditions. At a low slenderness and under a concentric axial load, the failure was characterized by splitting longitudinal cracks and or localized crushing leading to buckling of longitudinal reinforcement. At a relatively high slenderness and under an eccentric axial load, the failure was characterized by flexural tensile cracking and compressive crushing concentrating around the midspan of the specimens. As the slenderness increased, the capacity of specimens decreased with increasingly pronounced nonlinearity at the outset of the loading. The comparison with the code values showed that while CSA S304 underestimates the ultimate capacity in general, the ultimate capacity estimated by TMS 402/602 were much closer to the test results, especially for eccentrically loaded columns. This is attributed to a better estimate of the effective flexural rigidity by TMS 402/602.

The numerical results on a wide range of slenderness further confirmed the findings of the experimental program. The axial load-bearing capability of reinforced concrete block masonry columns decreases as their effective slenderness increases. The rate of this decease is associated with the applied load eccentricity. As eccentricity increases, the decrease due to an increase in slenderness is not as pronounced as in the low eccentricity case. Overall, CSA S304 tends to underestimate the capacity. However, for low slenderness and high eccentricity, CSA S304 performed reasonably well. For specimens with an effective slenderness greater than 30, the FE axial load capacity was significantly greater than that specified by of CSA S304. On the other hand, TMS 402/602 performed better than S304 in predicting ultimate capacity over a range of slenderness and eccentricity ratios.

List of Abbreviations and Symbols Used

Abbreviations

ASTM	American society for testing and materials
CMU	Concrete masonry unit
COV	Coefficient of variation
CSA	Canadian standards association
DAQ	Data Acquisition System
FE	Finite Element
LP	Linear potentiometer
LVDT	Linear variable differential transformer
MC	Medium height column built with C shaped blocks
MS	Medium height column built with stretcher blocks
RC	Reinforced concrete
SC	Short column built with C shaped blocks
SG	Strain gauge
SP	String pod

SS	Short column built with stretcher blocks
TC	Tall column built with C shaped blocks
TMS	The masonry society
TS	Tall column built with stretcher blocks

Symbols

A_e	Effective cross-sectional area of masonry
A_s	Area of tension longitudinal reinforcement
A_s'	Area of compression longitudinal reinforcement
b	Length of the wall
C_m	Moment gradient factor
c	Depth of the compressive part of cross section
d	Effective depth of the cross-section
d'	Distance between the tension reinforcement and the nearest section face
E	Modulus of elasticity
EI_{eff}	Effective flexural stiffness/rigidity
E_m	Modulus of elasticity of masonry

e	Virtual/actual eccentricity
e_1	The smaller virtual eccentricity occurring at the top or bottom of column
e_2	The larger virtual eccentricity occurring at the top or bottom of column
e_k	The kern eccentricity for the effective cross-sectional area
F_y	Yield strength of longitudinal reinforcement
F_t	Ultimate strength of longitudinal reinforcement
f_{yh}	Tensile strength of ties
f_m	Masonry compressive stress
f'_m	Compressive strength of masonry normal to the bed joint
h	Unsupported height of a wall or column
h''	Dimension of the confined grouted core in the cross-section
I	Moment of inertia
I_{cr}	Moment of inertia of the cracked section
I_{eff}	Effective moment of inertia of the cracked section
I_{end1}, I_{end2}	Net section moments of inertia at the ends considering eccentricity

I_n	Moment of inertia of column's uncracked section
I_o	Moment of inertia of the effective cross-sectional area
K	Lateral reinforcement factor in Pristley and Elder model
k	Effective length factor for compression member
M_1	The smaller factored end moment in a compression member
M_2	The larger factored end moment in a compression member
M_{cr}	Column's cracking moment capacity
M_{fp}	maximum primary moment of the member under initially applied loads
M_{ftot}	Design moment including the slenderness effect
M_p	Maximum primary moment
M_u	Magnified moment
$M_{u,o}$	Non-magnified strength level moment
M_{ult}	Ultimate moment capacity of column
P	Compressive axial load applied to the column in tests
P_0	Axial capacity derived from prism tests with flat end conditions

P_{cr}	Critical buckling load of the column in moment magnification method
P_{cr}	Cracking axial load of columns in test results
P_e	Column's Euler buckling axial compressive load
P_f	Total factored axial load
P_u	Factored axial load
P_{ult}	Ultimate axial load bearing capacity of specimens and archetypes
R	Reduction factor for elastic flexural rigidity
S_e	Section modulus of effective cross-sectional area
s_h	Spacing of the ties
t	Thickness of a wall or column
u_1	Distance between the applied load and compressive face of the member
Z_m	Slope of the stress-strain curve's linear post peak branch
β_d	Area ratio of cut off reinforcement to total area of tension reinforcement
Δ	Lateral deformation at midspan of eccentrically loaded columns
Δ_{ult}	Deformation corresponding to peak axial load
δ	Moment magnification factor in CSA S304-14

ε	Masonry compressive strain
$\varepsilon_1, \varepsilon_2$	Strain at compression and tension faces
ε_{ult}	Curvature corresponding to peak moment
ρ_s	Longitudinal reinforcement ratio
ϕ_{er}	Resistance factor for member stiffness
ϕ_m	Resistance factor for masonry
ψ	Moment magnification factor in TMS 402/602-14

Acknowledgements

Dr. Liu's persistent encouragement and insights propelled me forward during challenging times. Her mantra — to be steadfast, pragmatic, and diligent — has left an indelible mark on me. I've imbibed from Dr. Liu the belief that there's always scope for refinement in engineering and scientific endeavours, a principle I intend to uphold throughout my career.

My heartfelt gratitude extends to my committee members, Dr. Pedram Sadeghian and Dr. Dmitry Garagash. Their keen insights and invaluable feedback have significantly enriched my research.

A special thanks to Mr. Jordan Maerz and Mr. Jesse Keane for their unwavering commitment to assisting with the experimental program in the lab. Their expertise was instrumental to the project's success.

I'm indebted to Mr. Andrew Smith for his generosity in providing essential materials and a professional mason. His insights and expertise greatly enriched the experimental aspect of my work.

On a personal note, the journey through this academic venture was made bearable, thanks to the love and unwavering support of my family and friends. Their consistent encouragement, inspiration, and resilience provided the necessary strength. Particularly, my wife, Sadaf, has been a pillar of strength throughout this endeavour. Her ceaseless support and unwavering love have been pivotal in seeing this thesis through to its completion.

Chapter 1 Introduction

1.1 Masonry Columns

Masonry materials are primarily used in the construction of compressive elements in modern building construction, either as columns or walls. The fundamental difference between masonry columns and walls lies in their geometry. A masonry column is defined as a vertical compression member with a height greater than 5 times its thickness and a length less than 3 times its thickness (CSA S304.1-14). While both clay bricks and concrete masonry blocks are the primary materials for masonry construction, this study focuses on the latter due to its more common use in structural applications in North America. Masonry columns are required to be reinforced due to their structural significance to overall building stability, and they are structurally similar to reinforced concrete (RC) columns in resisting compressive load. However, the distinctive differences in material and geometry between them make them essentially two different structural elements. While the concrete columns are cast as a monolithic unit, masonry columns are composed of masonry blocks, mortar, and grout, each of which has its own material properties. Due to its modular nature, masonry columns can have multiple configurations of block arrangement to achieve the same cross-section. As shown in Figure 1.1, three different configurations of a column cross-section can be achieved using hollow concrete blocks, concrete C-shaped block units, and solid units. In all cases, masonry grout is cast into the cavity to form the bond between the steel reinforcement and the masonry units. It is conceivable that different configurations will lead to different behaviour characteristics.

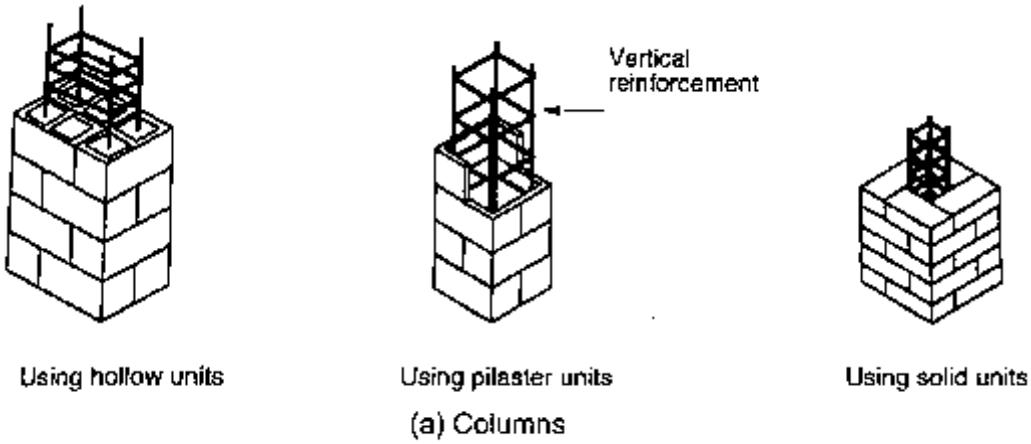

Figure 1.1. Reinforced masonry column construction (Drysdale & Hamid, 2005).

1.2 Research Motivation

While previous studies on RC columns are extensive in the literature, few experimental studies have been reported on the behaviour and failure mode of masonry columns. Hence, the development of design methods for masonry columns has relied on the background information for masonry walls, and RC columns to a lesser extent.

Among the few studies on masonry columns, experimental research conducted by Sturgeon, et al., (1971) and Edgell & Templeton (1985) are the most cited works in describing the failure mode of masonry columns. They showed that the failure of masonry columns is mainly dependent on factors such as whether the column is reinforced and the slenderness of the columns. While vertical splitting and crushing of the masonry shell and grouted core often govern the failure of unreinforced columns, face-shell spalling and buckling of the vertical reinforcement often characterize the failure of reinforced columns.

As the slenderness of the column increases, the above-mentioned failure occurs at a lower axial load because of the increased bending moment due to the slenderness effect, also referred to as the P-Δ effect (Drysdale & Hamid, 2005).

For design, the slenderness effect is considered using the moment magnifier method in the current Canadian masonry design standard (CSA S304-14). Based on the Euler buckling concept, the moment magnifier method is a simple, one-step calculation to approximate the secondary moment due to the slenderness effect. The elastic flexural rigidity EI in the Euler buckling concept is replaced by an effective flexural rigidity EI_{eff} to account for the cracking of masonry and yielding of the steel reinforcement of the masonry column. The accuracy in EI_{eff} thus plays a critical role in the effectiveness of the moment magnifier method. The current design equations for EI_{eff} in CSA S304 for both masonry columns and walls are essentially the same. The existing provisions for masonry walls were developed more than 40 years ago based on limited experimental data. However, little to no background information is attributed to masonry columns. The available information (or lack thereof) on the design of the slenderness effect suggests that the EI_{eff} expression for masonry columns was simply transferred from that for masonry walls. Previous studies (Liu 2002, Isfeld, et al. 2019) showed that the EI_{eff} equation for masonry walls underestimates the flexural rigidity of masonry walls, leading to overly conservative design. The validity of the equation for application in masonry columns has not been investigated, and no experimental data on masonry columns are available in the literature to support or oppose the observation made for walls. For the American masonry design standard (TMS 402/602-16), while the moment magnifier method also applies, the EI_{eff} equation contained in that standard is distinctively different from CSA S304. Thus, the

Canadian and American masonry standards would yield different masonry column designs for the same set of material properties and loading conditions.

1.3 Research Objectives

This study aims to study the behaviour and capacity of reinforced masonry columns, and specifically to investigate the flexural rigidity and its application in the moment magnifier method in the design of reinforced masonry columns.

The following activities were performed to achieve this objective:

Activity 1: Conduct an experimental study on RM columns with design parameters including slenderness ratio, cross-section configuration, and applied eccentricity of axial load.

Activity 2: Develop a finite element model capable of simulating the behaviour and capacity of RM columns with various material and geometric properties.

Activity 3: Compare the FE model results with the experimental results.

Activity 4: Evaluate the validity of the moment magnifier method of CSA S304-14 and TMS 402/602.

1.4 Thesis Layout

This thesis is organized as follows.

Chapter 1 or the present chapter that introduces the masonry columns and the objectives of this research project.

Chapter 2 presents the literature review related to this study.

Chapter 3 includes details of the experimental program, covering specimens' properties and construction steps, a well as the test setup.

Chapter 4 presents information on the results of the experimental program including observed failures, load-deformation, and moment curvature relationships and compares these results with those of CSA S304 and TMS 402/602.

Chapter 5 explains the numerical modeling methodology and the verification of the model with test results.

Chapter 6 contains information on the parametric study conducted by the numerical model, comparing those results with predictions of the CSA S304 and TMS402/602, and offers further discussions.

Chapter 7 presents a summary of the results of this research projects, conclusions, and recommendations for future research projects in this field.

Chapter 2 Literature Review

2.1 Introduction

This chapter presents a state-of-the-art review on the research and design of reinforced masonry columns. As mentioned earlier, limited research has been conducted and reported specifically on masonry columns; instead**,** most available studies on the general subject of masonry compression elements focus on masonry walls. The following sections aim to provide the most relevant information on the current research and design practice of reinforced masonry columns.

2.2 Slenderness Effect

The most important aspect of the design of structural compression members is the consideration of the slenderness effect. In essence, as the slenderness of a compression member increases, its axial capacity is increasingly governed by buckling failure as opposed to material failure. The effect of slenderness was first studied on the brick masonry walls by Yokel, et al. (1970), Hasan & Hendry (1976), and Fattal & Cattaneo (1976). Yokel & Dikkers (1971) and Hatzinikolas, et al. (1978) respectively carried out a series of tests on a number of masonry walls, using both brick and concrete masonry. They suggested that the moment magnifier method can be adopted in predicting the load-carrying capacity of masonry walls and stressed that the critical buckling load must account for the effect of loading conditions, tensile strength of masonry, and type of construction (reinforced or plain). The moment magnifier method, based on the Euler buckling concept, was first developed for steel structures. Its adoption for structural elements made of brittle materials was first applied to reinforced concrete structures and then to reinforced masonry

structures. Currently, the use of the moment magnifier method to account for the slenderness effect is widely adopted in various codes and standards, including the Canadian and American masonry design standards. The tensile cracking and steel yielding, which are typical behaviours when dealing with brittle materials, are intended to be considered in the calculation of the critical buckling load through a so-called effective flexural rigidity, EI_{eff}.

2.3 North American Design Practice

While both the Canadian and American masonry design standards have adopted the moment magnifier method as a framework to consider the slenderness effect, the provisions for the evaluation of EI_{eff} in the two standards deviate markedly. This results in disparity in design using these two standards. The following section describes the slenderness effect treatment in both standards.

2.3.1 CSA S304-14 Design of Reinforced Masonry Columns

CSA S304 stipulates that the moment magnifier method can be used to consider the effect of slenderness on compression members, where the design moment is magnified to account for the secondary effect through a first-order analysis as follows:

$$M_{fiot} = M_{fp} \frac{C_m}{\left(1 - \frac{P_f}{P_{cr}}\right)} \geq M_{fp} \tag{2.1}$$

$$P_{cr} = \frac{\pi^2 \phi_{er} \left(EI\right)_{eff}}{\left[\left(1 + 0.5\beta_d\right)\left(kh\right)^2\right]} \tag{2.2}$$

$$C_m = 0.6 + 0.4\frac{M_1}{M_2} \tag{2.3}$$

where M_{ftot} is the design moment including the slenderness effect, M_{fp} is the maximum primary moment of the member due to the initially applied loads, and P_f is the total factored axial load in the column. The moment magnification, as a result of the slenderness effect, is considered through the moment magnification factor $C_m/(1-P_f/P_{cr})$. In this factor, C_m is the moment gradient factor, which is used to convert the actual moment diagram to an equivalent uniform moment diagram. As C_m does not involve the material properties and is based on the distribution of external moments, the expression C_m is universally the same for RM, RC, and steel columns, and is well established in the design standards. P_{cr} is the critical buckling load of the column, where the flexural rigidity EI_{eff} is the deciding factor of this quantity.

CSA S304-14 provides the following equation for calculating EI_{eff}.

$$EI_{eff} = E_m\left[0.25I_o - \left(0.25I_o - I_{cr}\right)\left(\frac{e-e_k}{2e_k}\right)\right] \tag{2.4}$$

and the value of EI_{eff} shall not be greater than $0.25E_mI_o$, but need not be taken less than E_mI_{cr}. E_m is the modulus of elasticity of masonry, I_o is the moment of inertia of the uncracked effective cross-sectional area of the column, I_{cr} is the transformed moment of inertia of the cracked section, e is the equivalent applied eccentricity, and e_k is termed the kern eccentricity = S_e/A_e where S_e is the section modulus of the effective cross-sectional area (A_e).

In accordance with the CSA S304 guidelines, slenderness effects can be disregarded when the ratio kh/t falls below $(10 - 3.5(e_1/e_2))$. Here, k represents the effective length factor, h stands for the unsupported column height, and t denotes the column thickness. Additionally, e_1 signifies the smaller virtual eccentricity observed at one column end, while e_2 points to the greater virtual eccentricity at the opposite end.

The CSA S304 stipulates that if the kh/t ratio is 30 or less, it's mandatory to adopt the procedures outlined in the p.δ or the moment magnifier methods. This ensures proper consideration of slenderness effects. The code also clearly establishes a maximum permissible kh/t value of 30 for columns, mandating that the creation of masonry columns with a kh/t exceeding this value is not permissible.

Contrastingly, the code allows the design and erection of masonry walls with a kh/t surpassing 30, but only if the axial load-bearing capacity remains restricted to $0.1\phi_m f'_m A_e$. This provision acknowledges the heightened risk of buckling in extremely slender walls. A contentious point raised earlier in this chapter revolves around the prohibition by CSA S304 on the design and construction of extremely slender masonry columns, irrespective of their reinforcement status. This stands in contrast to the code's allowance for walls with equivalent slenderness ratios, provided a maximum load-bearing capacity is maintained.

2.3.2 TMS 402/602-16 Design of Reinforced Masonry Columns

The American masonry code (TMS 402/602) uses a similar approach for calculation of the magnified moment, but proposes a different equation for EI_{eff}. While the CSA S304 prohibits the design and construction of masonry columns more slendered than kh/t = 30, the TMS code does not impose such a limit.

TMS 402/602 stipulates that the moment magnifier method can be used to consider the effect of slenderness in the design of axially compressed members, where the strength level moment shall be determined using the moment magnification equation as follows:

$$M_u = \psi M_{u,0} \tag{2.5}$$

where $M_{u,0}$ is the non-magnified strength level moment from the first-order analysis, ψ is the moment magnification factor, and M_u is the magnified moment. The moment magnification factor, ψ can be determined as follows:

$$\psi = \frac{1}{1 - \frac{P_u}{P_e}} \tag{2.6}$$

where P_u is the factored axial load on the column and P_e is the column's Euler buckling axial compressive load which is determined using the following equation:

$$P_e = \frac{\pi^2 E_m I_{eff}}{h^2} \tag{2.7}$$

where I_{eff} is the effective moment of inertia of the cracked section. I_{eff} shall be taken as $0.75I_n$ for $M_u < M_{cr}$ and shall be taken as I_{cr} for $M_u \geq M_{cr}$. In these relationships, I_n is the uncracked moment of inertia of the columns' cross section, I_{cr} is the cracked cross section moment of inertia, and M_{cr} is the column's cracking moment capacity under bending. It should be pointed out that TMS 402/602 takes into account the compressive load effect when calculating I_{cr} whereas CSA 304 calculates I_{cr} ignoring the compressive load effect.

2.4 Research on EI_{eff}

The CSA S304-14 provides little background information on how the EI_{eff} expression was proposed and calibrated, especially when it comes to its application in RM columns. What is known is that the expression was initially suggested for masonry walls and thus some important research around slenderness effect and EI_{eff} for walls as described in the following.

Yokel & Dikkers (1971) were among the first to develop an effective Euler buckling load expression for the case of a cracked member subjected to compression under equal end eccentricities, as shown in Eqn 2.8. They assumed the material to have no tensile strength and to exhibit a linear stress-strain relationship in compression.

$$P_{cr} = 0.64 \frac{\pi^2 E b u_1^3}{h^2} \tag{2.8}$$

Further, Yokel also proposed the following equation for the flexural rigidity of masonry walls at failure.

$$EI = E_m I_o \left[0.2 + \frac{P}{P_0} \right] \leq 0.7 E_m I_o \tag{2.9}$$

In the above equations, b is the length of the wall, u_1 is the distance between the applied load P and the compressive face of the member at the ends, h is the height of the wall, and P_0 is the axial capacity derived from prism tests with flat end conditions.

The accuracy of Yokel and Dikkers equations was examined by Fattal & Cattaneo (1976) to investigate possible applications of these equations in concrete masonry walls. They tested eccentrically loaded short columns and using a moment-curvature relationship, they proposed an equation for the flexural rigidity, EI as follows.

$$EI = \frac{Pet}{\varepsilon_1 - \varepsilon_2} \tag{2.10}$$

where t is wall thickness, P is the axial load, e is the axial load eccentricity with respect to the cross-section centroid, and ϵ_1 and ϵ_2 are wall strains at compression and tension faces respectively. Fattal & Cattaneo compared EI values from their equation with results from Yokel & Dikkers (1971) eqaution for both brick and concrete masonry walls and noticed that Yokel & Dikker's equation underestimated Ei for concrete block specimens. It is important to note that Fattal & Cattaneo (1976) did not consider secondary moment effects into account in their equation.

Hatzinikolas, et al. (1978) studied 68 full scale reinforced and unreinforced masonry walls of various slenderness ratios (kh/t) ranging from 5 to 22 subjected to combinations of axial loads and end moments. Using the solution for elastic deflection curve of a wall, they showed that for eccentricities less than t/3, the moment of inertia and the buckling load for hollow or solid cracked sections can be approximated by the following equations, respectively.

$$I = 8\left[\frac{1}{2} - \frac{e}{t}\right]^3 I_o \tag{2.11}$$

$$P_{cr} = 8\pi^2 \left(\frac{1}{2} - \frac{e}{t} \right)^3 \frac{EI_o}{h^2} \tag{2.12}$$

In this equation, e is the eccentricity of the applied axial load. These equations were based on a linear stress-strain assumption for masonry and single curvature bending with equal end eccentricities.

As both Yokel and Hatzinikolas et al.'s equations were based on linear stress distribution of a cracked section, strictly speaking, both equations were only valid for unreinforced masonry where tension cracking could govern the failure.

Ojinaga & Turkstra (1982) proposed the following equations for definition of the effective moment of inertia near failure for reinforced masonry members.

(a) For single curvature bending

$$I_{eff} = \frac{1}{4}\left(I_{end1} + 2I_{cr} + I_{end2} \right) \tag{2.13}$$

(b) For double curvature bending

$$I_{eff} = \min\left\{ \frac{1}{4}\left(I_{end1} + 2I_{cr} + I \right), \frac{1}{4}\left(I_{end2} + 2I_{cr} + I \right) \right\} \tag{2.14}$$

I_{end1} and I_{end2} are the net section moments of inertia at the ends taking eccentricity into account and I is the minimum net section moment of inertia including the contribution, if any, of steel area transformed to equivalent masonry. They suggested that the effective moment of inertia of a member should be evaluated considering the combined effect of the ends and minimum net section. Compared with test results, these equations were found to

be conservative especially for symmetrical single curvature loading cases (Ojinaga & Turkstra, 1982).

Maksoud & Drysdale (1993) conducted a numerical investigation of slender unreinforced hollow concrete masonry walls and proposed that the effective flexural rigidity EI_{eff} can be determined by applying a reduction factor R to the elastic flexural rigidity EI_o. Using a statistical program, a regression analysis was carried out for cases of single curvature (e_1/e_2 = 1 and 0) and double curvature (e_1/e_2 = -1) and the resulting equations for the reduction factor R are as follows:

(a) For single curvature

$$R = 0.1037 + 0.915\frac{e}{t} + 0.089\frac{e}{t}\left(\frac{e_1}{e_2}\right) + 0.00034\left(\frac{h}{t}\right)^2 - 0.0098\frac{e}{t}\left(\frac{h}{t}\right) \tag{2.15}$$

(b) For double curvature

$$R = 0.3278 - 1.98\frac{e}{t}\left(\frac{e_1}{e_2}\right) + 0.0425\frac{e}{t}\left(\frac{h}{t}\right) + 0.00044\left(\frac{h}{t}\right)^2 - 0.0146\left(\frac{h}{t}\right) \tag{2.16}$$

In these expressions, R increases with increasing e/t and with increasing h/t. The formulations represent an empirical approach, which requires additional verification. Consequently, Maksoud & Drysdale (1993) suggested that the influences of section geometries, material properties, reinforcing and long-term effects be incorporated.

Liu & Dawe (2003) tested 36 reinforced concrete masonry walls to investigate the behaviour of masonry walls under combined axial and lateral loading. Test results showed that the EI_{eff} differs from the results of CSA S304.1-14 in cases where compression failure

tends to predominate. They proposed the following equation as a lower bound bilinear limit for the EI_{eff} of reinforced masonry walls based on approximately 500 computer model tests.

(a) For $0.0 \leq e/t \leq 0.4$

$$EI_{eff} / EI_o = 0.80 - 1.95\left(1.00 - 0.01h/t\right)\left(e/t\right) \tag{2.17}$$

(b) For $e/t \geq 0.4$

$$EI_{eff} / EI_o = 0.022\left(1.00 + 0.35h/t\right) \tag{2.18}$$

where e is the maximum end eccentricity for end-applied axial loads. For combined axial and lateral loads, e is equal to M_p/P, where M_p is the maximum primary moment and P is the applied axial load.

Liu & Hu (2007) tested 12 reinforced masonry wall specimens under eccentric compressive loading with varying eccentricity to thickness ratio e/t, and end eccentricity ratios e_1/e_2. All specimens were simply supported at both ends and had a slenderness of 17.1. They found that the variation of ultimate load, P_u, and effective modulus of rigidity EI_{eff} at failure depended on the type of failure mode, which was influenced by e/t and e_1/e_2 ratios and their interactions. They found that the CSA S304 underestimates EI_{eff} values, especially in regions where compression-controlled failure tends to predominate which leads to conservative design.

Popehn, et al. (2008) investigated the buckling behaviour of slender (h/t=38) unreinforced masonry walls subjected to axial compression and out-of-plane lateral loads through an experimental program. They also used a finite element model to validate their tests. One of

the findings of their study was that the predicted strength of walls by the CSA S304 is less than the actual strength of wall.

Isfeld, et al. (2019) tested three concrete masonry walls with kh/t of 12.6 to investigate the effect of end conditions on design of slender concrete masonry walls. They found that the behaviour of concrete masonry walls was greatly affected by support conditions at the base of the wall and the pinned-pinned support conditions from the previous studies was not accurate as representation of the reality. They suggested that the provisions for slender walls in the CSA S304.1-14 need to be re-examined to ensure more efficient use of masonry.

Chapter 3 Experimental Program

3.1 Introduction

The experimental program involved testing of reinforced concrete masonry column specimens as well as associated masonry materials and prisms. Six masonry column specimens were tested under concentric or eccentric compression to failure. Auxiliary tests were conducted concurrently to obtain the material properties of concrete masonry units (CMUs), mortar, grout, reinforcing steel, and masonry prisms. The following sections provide a detailed description of the column specimens, their fabrication process, and the test setup and procedure, while the associated auxiliary tests are presented in Appendix A.

3.2 Column Specimens

Figure 3.1. Experimental program cross section configurations. (a) Stretcher Blocks; (b) C-Shaped Blocks

Table 3.1 summarizes the six masonry column specimens tested in the program. Design parameters considered included effective slenderness ratio, kh/t, axial load eccentricity, e/t, and end eccentricity ratio, e_1/e_2. The six specimens were divided into three groups based on their height, resulting in three slenderness ratios: short (S), intermediate (M), and tall (T). It needs to be pointed out that, in practice, a slenderness ratio close to 30 is permitted for a masonry column. However, a height of 3 meters is the maximum height that can be accommodated in the Heavy Structures laboratory and thus, the slenderness of 15.8 represents the limit achieved with the laboratory conditions and a label of “T” was used here for these specimens.

Within each group, two different column cross-section configurations were studied, as depicted in Figure 3.1. Both configurations are utilized in practice depending on the purpose and functionality of the columns, and were thus examined in this study. Specimens made of stretcher blocks are labeled with "S" and those made of C-shape blocks are labeled with "C". For example, specimen SS indicates a specimen with a short slenderness and constructed with stretcher blocks. M#10 steel rebar was used as longitudinal reinforcement and 3.65 mm steel wire as confinement ties.

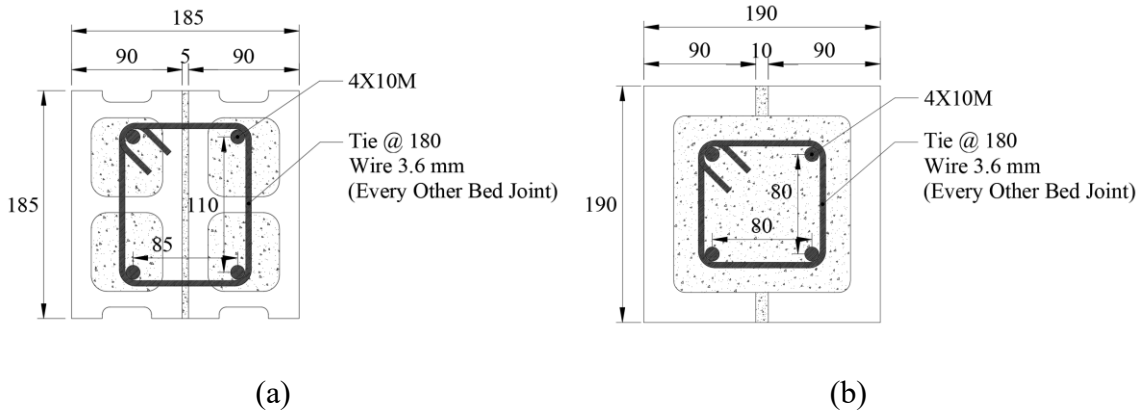

Figure 3.1. Experimental program cross section configurations. (a) Stretcher Blocks; (b) C-Shaped Blocks

Table 3.1. Reinforced concrete masonry specimens.

Number	Specimen ID	Height (mm)	Effective Slenderness Ratio (kh/t)	Cross Section Configuration	Axial Load Eccentricity (e/t)	Eccentricity Ratio (e_1/e_2)
1	SC	1200	6.3	C-Shaped Blocks	0	0
2	SS	1200	6.3	Stretcher Blocks	0	0
3	MC	2400	12.6	C-Shaped Blocks	1/3	+1
4	MS	2400	12.6	Stretcher Blocks	1/3	-1
5	TC	3000	15.8	C-Shaped Blocks	1/3	+1

6	TS	3000	15.8	Stretcher Blocks	1/3	+1

Concentrically loaded columns had an e/t ratio of zero. For those loaded eccentrically, the e/t ratio of 1/3 was used which corresponded to an eccentricity of 63.3 mm measured from the centre of the column cross-section. Based on the principles of mechanics, this eccentricity will generate a high tensile stress on the column cross-section, thus resulting in tensile cracking along the height of the column. The results were expected to demonstrate the effect of cracking on the flexural rigidity and capacity of columns.

Lastly, for those four eccentrically loaded specimens, three were tested under single curvature bending ($e_1/e_2=1$) and one was tested under a reverse curvature bending ($e_1/e_2=-1$). All parameters are further illustrated in Figure 3.2.

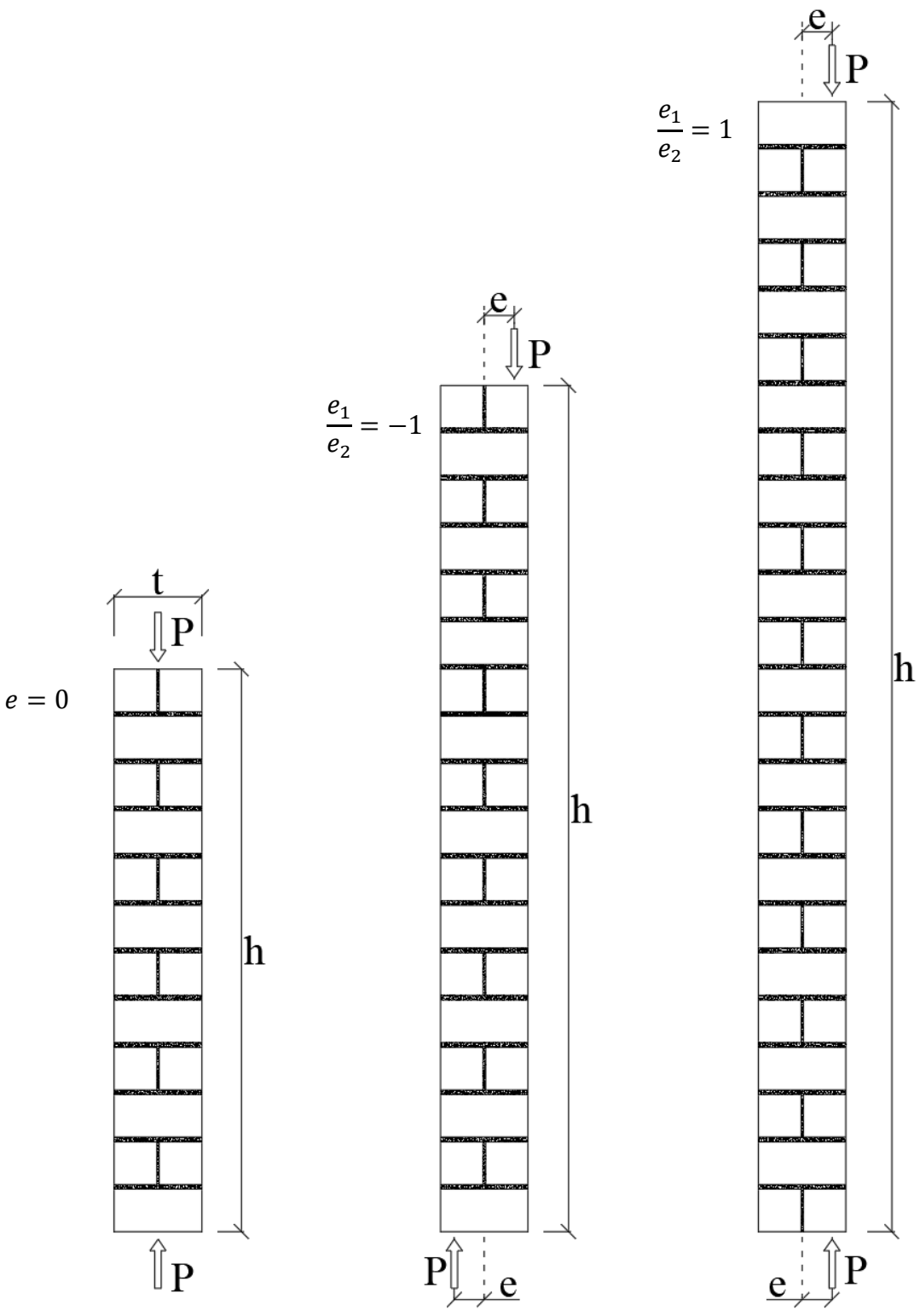

Figure 3.2. Design parameter illustration

3.3 Construction of Column Specimens

The masonry column specimens were constructed by a certified mason in the Heavy Structures Laboratory of the Department of Civil and Resource Engineering at Dalhousie University in January 2023.

These specimens were constructed and cured in an upright position. For all specimens, an initial bed joint was placed first, and the blocks for each course were placed thereafter. Type S mortar, as outlined in the Mortar and Grout for Unit Masonry standard (CSA A179-14), was provided on all surfaces of the block. Pre-bent column ties were secured around the longitudinal reinforcements at the joint level of every other course. A plumb line and a level were used to ensure each course was levelled and the column was plumb after each course was laid. After laying the courses to the specimen's desired final height, grouting was conducted using high slump grout as per CSA A179-14. Figure 3.3 displays the specimens with grout in place and while Figure 3.4 presents all specimens post-construction. It is worth noting that the wooden framework, as seen behind the specimens, was designed to provide lateral support during construction and to aid in transporting the specimens to their testing positions. The extra lengths of steel rebars remained in place post-construction and during curing. They were cut off to the desired length prior to testing. Additionally, it should be highlighted that grouting for those columns made of stretcher blocks was found to be challenging. The cavities of blocks are narrow and the steel rebars and overflown mortar joints obstructed free flow of the grout. Even though the grout was made with a high slump and grouting was executed with consistent vibration, it remained difficult to ensure that all cavities were filled with grout throughout the entire height of the

specimens. In fact, one specimen was turned out to be defective with grout void in several courses, leading to its premature failure. Further details on this specimen are provided in Chapter 4.

(a) Before Grouting (C-shaped)

(b) Before Grouting (Stretcher)

(c) After grouting

Figure 3.3. Specimens construction before and after grouting.

Figure 3.4. Specimens after construction.

Specimens SS, MC, and TS were instrumented with four strain gauges on four longitudinal rebars at their mid-height to measure strains in the specimens during testing. For column MS, which was tested in reverse curvature, eight strain gauges were used: four were situated at 1/4h and the remaining four at 3/4h. This arrangement facilitated the collection of strain data at the critical cross-sections of the column under reverse curvature. The strain gauges were installed on the rebars before the construction of the columns commenced. The rebar surface was meticulously prepared for the application of the strain gauges (Figure 3.5). This was followed by the application of a protective coating and the final wrapping of the strain gauges (Figure 3.5).

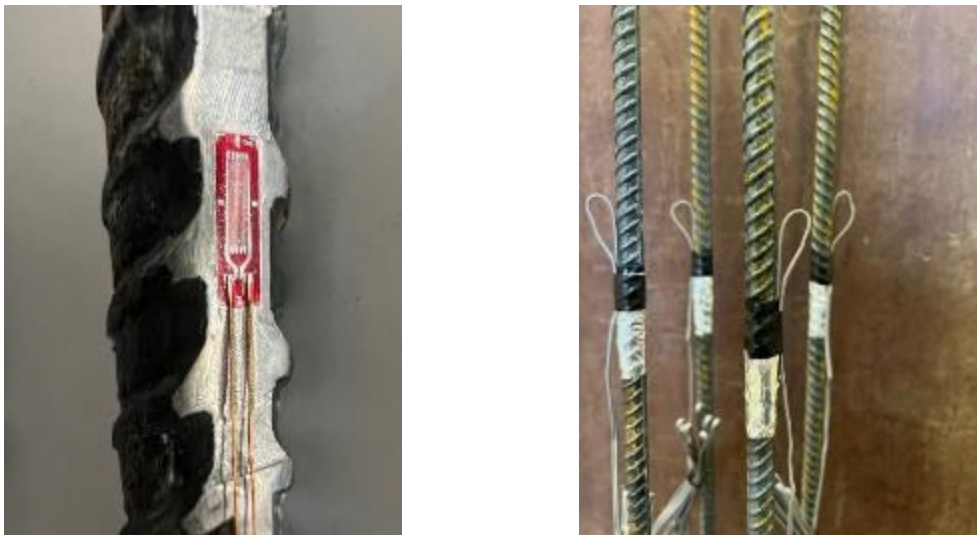

(a) Before coating (b) After coating

Figure 3.5. Strain gauge installation.

Once the construction of all columns was completed, they underwent a curing process lasting 28 days. This process involved regular water spraying, followed by covering the columns to retain the moisture, thereby ensuring optimal curing conditions (as depicted in Figure 3.6).

Figure 3.6. Curing of columns using water spray and plastic coverings.

3.4 Tests Setup

The masonry column specimens were tested in a horizontal position using a 2 Mega Newton actuator in the Heavy Structures lab. Figure 3.7 provides a schematic plan view of the entire testing assembly and Figure 3.8 presents a photo of the test setup. Two concrete blocks, anchored to the strong floor using steel rods, served as reaction points for the specimen when the load was applied. The ends of the specimens were housed in a built-up plate assembly forming a “shoe”. Grout bags were used between the columns' ends and the steel plate assembly to ensure a uniform distribution of the load across the column cross-

sections, thereby preventing premature local crushing. The load was applied via a solid steel circular bar to the steel plate assembly at the specimen ends. Load eccentricity was achieved by positioning the steel bar to a pre-notched plate with the desired eccentricity. To offset the columns' self-weight when tested in a horizontal position, steel seat assemblies were positioned underneath the intermediate and tall specimens at 1/3h intervals from the bottom of the specimens. As illustrated in Figure 3.10, an assembly comprised a steel ball bearing and steel plates, with the ball bearing allowing the column to rotate about the horizontal axis. This type of setup was inspired by Khorramian & Sadeghian (2020) in their work on testing of reinforced concrete columns.

An electronic data acquisition system was deployed to monitor and record load, strain, and deformation data throughout the loading history. There were some differences in data collected from different specimens, but typically, lateral deformation was recorded at various points along the lengths of the columns using LPs and SPs. Additionally, strain of the reinforcement was measured at critical points of the columns. Movements of the testing rig relative to the floor were also recorded. Figure 3.9 depicts the instrumentation scheme for all specimens.

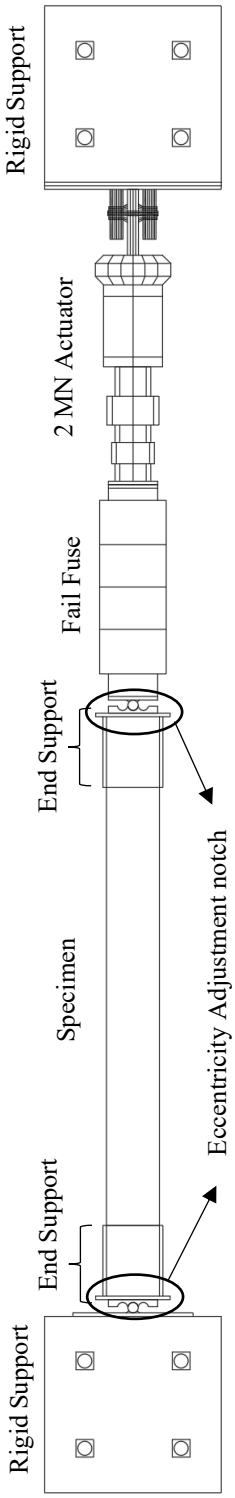

Figure 3.7. Test setup diagram.

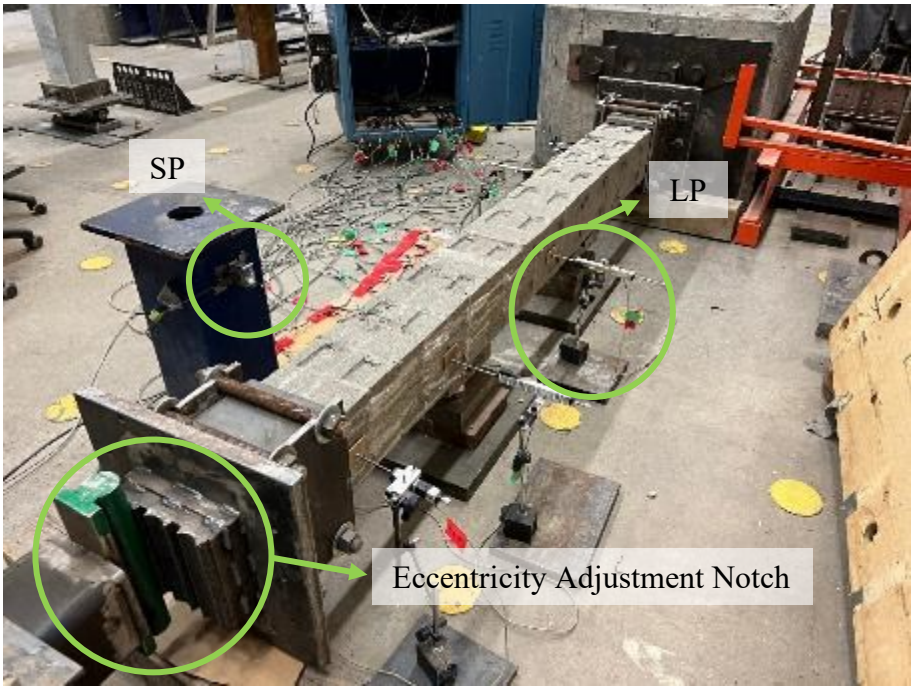

(a) Sample test setup of a column with instrumentation.

(b) 2 MN actuator and its rigid support.

(c) Rigid cubic concrete support.

Figure 3.8. Test setup.

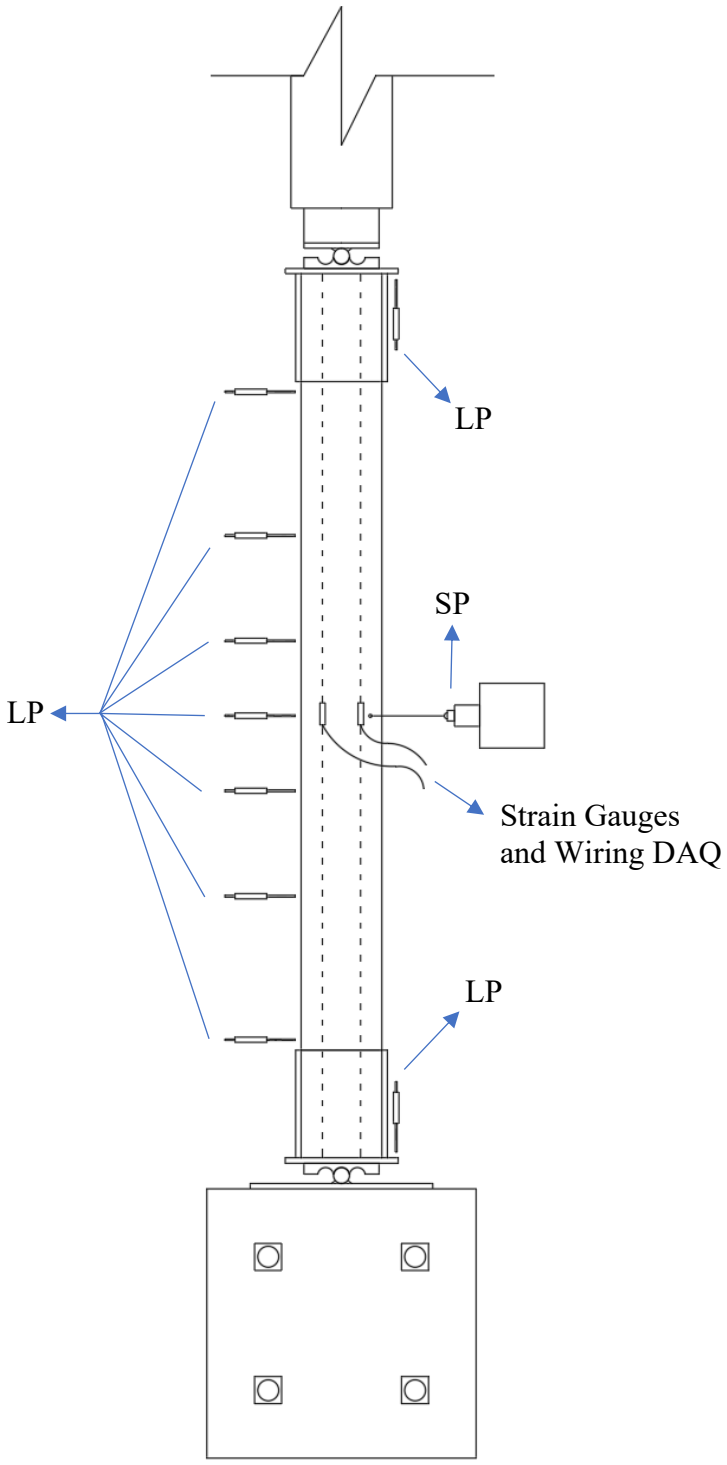

Figure 3.9. Typical instrumentation setup.

Figure 3.10. Steel balls for weight elimination.

3.5 Test Procedure

Before each test, the ends of the specimens were prepared where the extra length of the rebars was first cut off, and surfaces were ground to level if necessary. Each specimen was carefully transported and positioned in the testing setup. Grout bags were then positioned between the ends of each specimen and the loading plate assembly, referred to as the "shoes". The circular loading cylinder was adjusted to the desired loading eccentricity. Both the load cell(s) and displacement transducers were inspected to ensure they functioned properly and were zeroed at the commencement of the test. The loading rate was set at 0.4 mm/min until failure. Both the load cell and all LVDTs were configured to capture data at 0.1-second intervals using an electronic data acquisition system. During each test, the cracking pattern, ultimate load, and failure mode were continuously observed and documented.

Chapter 4 Experimental Program Results and Discussion

4.1 Introduction

This chapter presents the test results for the masonry columns, detailing their load-deformation behavior, moment-curvature relationship, and failure modes. Relevant design parameter effects are also discussed. While a summary of the results from the auxiliary tests concerning the masonry material properties is provided, detailed findings can be found in Appendix A.

4.2 Summary of Test Results

Table 4.1 provides a summary of the test results for column specimens, along with the masonry and steel rebar properties for each specimen obtained from auxiliary tests. It is noted that specimens constructed with stretcher blocks exhibited significantly lower masonry strength compared to those constructed with C-shaped blocks. Although the mortar and grout mix were used consistently for both constructions, the higher strength of the C-shaped block compared to the stretcher blocks, led to this pronounced difference in masonry strength.

Table 4.1. Test results of column specimens.

Specimen ID	Effective Slenderness Ratio (kh/t)	Masonry		Steel		P_{cr} (kN)	P_{ult} (kN)
		f'_m (MPa)	E_m (MPa)	F_y (MPa)	F_t (MPa)		
SC	6.3	18.5	15,856	381	571	583	675
SS	6.3	8.5	7,482			392	468
MC	12.6	20.5	17,061			149	244
MS	12.6	7.9	7,896			-	95
TC	15.8	19.3	15,547			141	212
TS	15.8	9.5	9,307			97	147

In general, for both concentrically loaded specimens SC and SS, failure began through splitting cracks of blocks under compression, followed by spalling of blocks and grout. Crushing of the grout core was the final mode of failure. For all eccentrically loaded specimens excluding MS, failure initiated by flexural cracking. Compression induced cracks on the compressive face of the column initiated on the shell units followed by debonding or block and grout and spalling. Tension induced cracks on the tensile face of the column initiated by debonding the mortar and blocks at bed joints. The failure of these specimens was marked by the crushing of the grouted core and buckling of the compressive longitudinal reinforcement at mid-span. The buckling of the longitudinal reinforcement was localized within the untied intervals. These specimens exhibited a pronounced curvature at failure. Specimen MS failed prematurely, and no final failure mode was observed.

4.3 Group "S" Specimens: SS and SC

These two specimens were 1200 mm high (kh/t = 6.3) and tested under concentric compression. They were used as control specimens to obtain the compressive capacity of columns when the slenderness is not a concern. Figure 4.1 show the comparison of axial load vs. axial deformation curves of specimens SS and SC. It can be seen that specimen SC, constructed with C-shaped blocks, had a higher capacity at both cracking and ultimate stages when compared to specimen SS constructed with stretcher blocks. This difference in capacity is expected as the masonry compressive strength f'_m for these two specimens was significantly different (8.5 vs 18.5 MPa). While attaining lower capacities, specimen SS exhibited greater deformations at cracking and ultimate than specimen SC, indicating a more ductile behaviour. Both specimens began to show noticeable cracking around 85% of the ultimate load, and the load vs. axial deformation curves remained more or less linear up to the cracking load, albeit that specimen SS showed a much lower stiffness. The failure occurred with significant cracking of masonry and buckling of axial reinforcement for both specimens. Figure 4.2 shows the overall failure modes and Figure 4.3 provides close-up photos showing localized failure of these two specimens. For specimen SC, cracking occurred through the C-shaped blocks, while the grouted core remained intact, and final failure was due to the buckling of the axial reinforcement. For specimen SS, cracking was more extensive, and final failure was due to crushing of grouted core and buckling of the reinforcement. Linear axial stiffness of specimens SC and SS were calculated to be 12,983 MPa and 7,384 MPa respectively, as the slope of the initial linear portion of load vs. deformation diagrams.

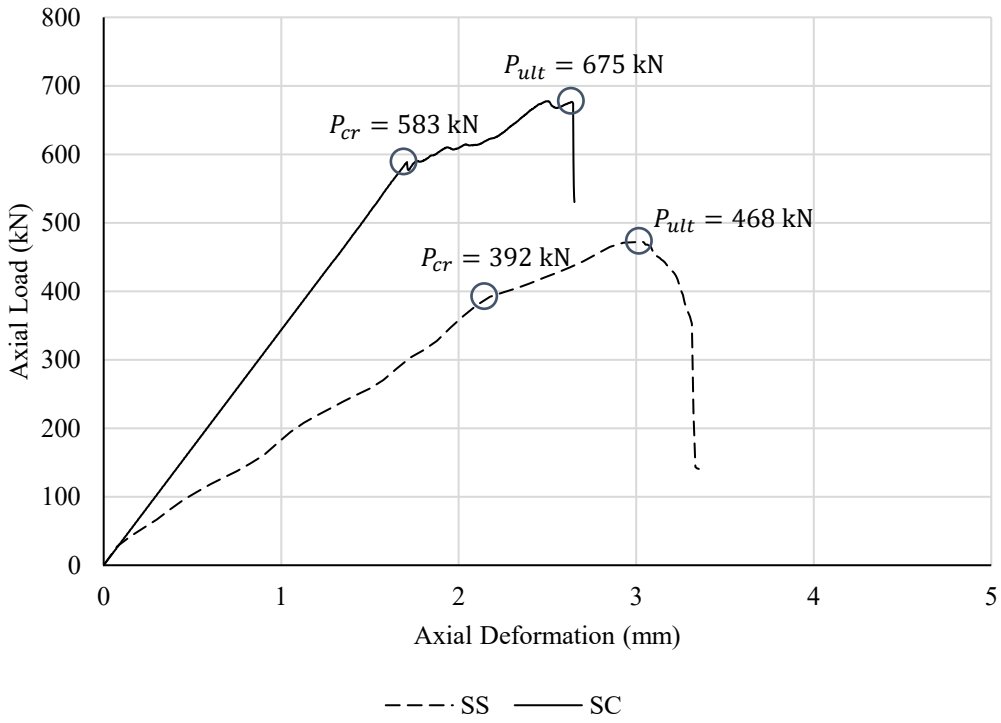

Figure 4.1. Comparison of load vs axial deformation diagrams of concentrically loaded specimens.

(a) specimen SC

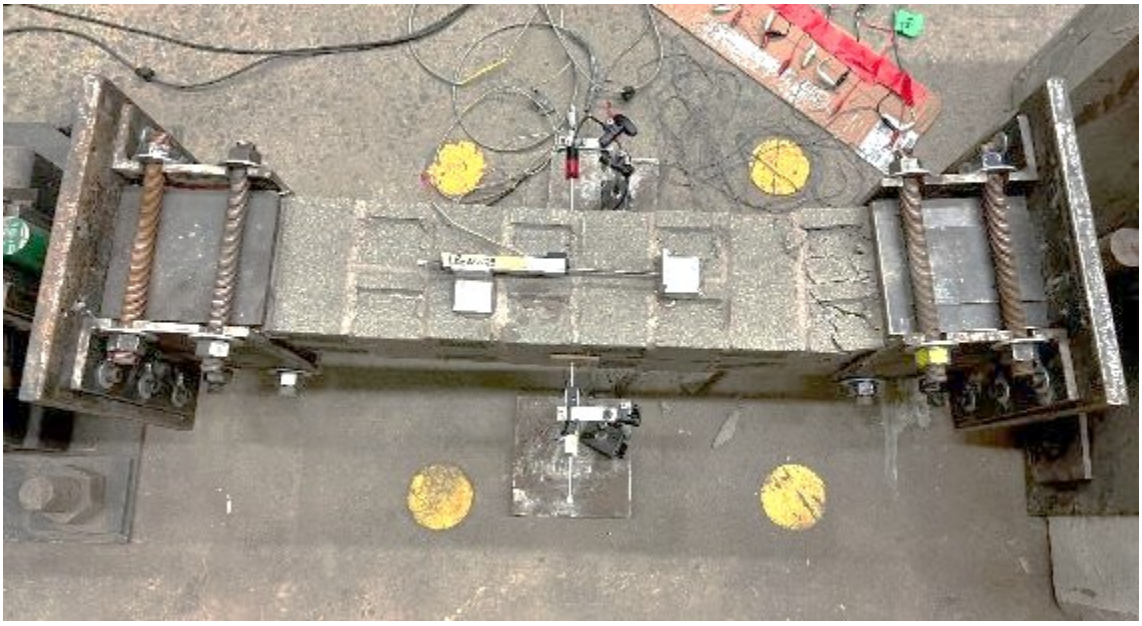

(b) specimen SS

Figure 4.2. Specimen SS and SC after failure.

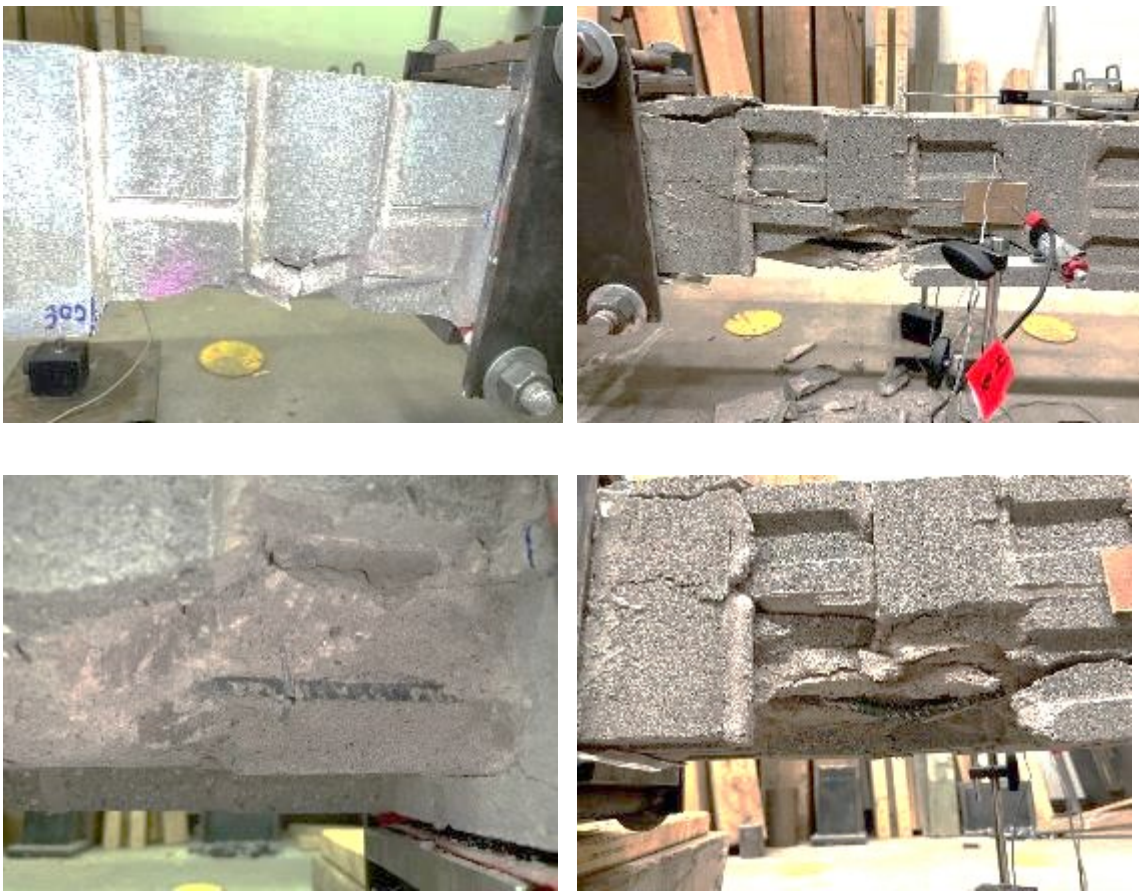

(a) specimen SC (b) specimen SS

Figure 4.3. Masonry crushing and longitudinal reinforcement's local buckling for specimens SC and SS.

4.4 Group "M" Specimens: MS and MC

These two specimens had a height of 2400 mm (kh/t=12.6) and tested with a load eccentricity of 1/3t in single curvature for MS and reverse curvature for MC. Figure 4.4 shows the load vs. lateral deformation obtained at midspan of specimen MC. The onset of nonlinearity began almost immediately after the application of load. This nonlinearity was largely attributed to the geometric nonlinearity resulting from additional deformation due to the secondary moment, a typical behaviour for beam-columns. At around P = 93 kN, flexural cracks began to appear at midspan on the tension side of the column. As the tensile crack extended through the midspan mortar joint, crushing began to occur on the compression side around the midspan. The crushing caused spalling of the face shell and splitting of grouted cores on the compression side. The specimen failed at a load of P_{ult} = 244 kN when the longitudinal compressive reinforcement buckled on the compression side of the specimen. The failure modes are shown in Figure 4.5 to Figure 4.7.

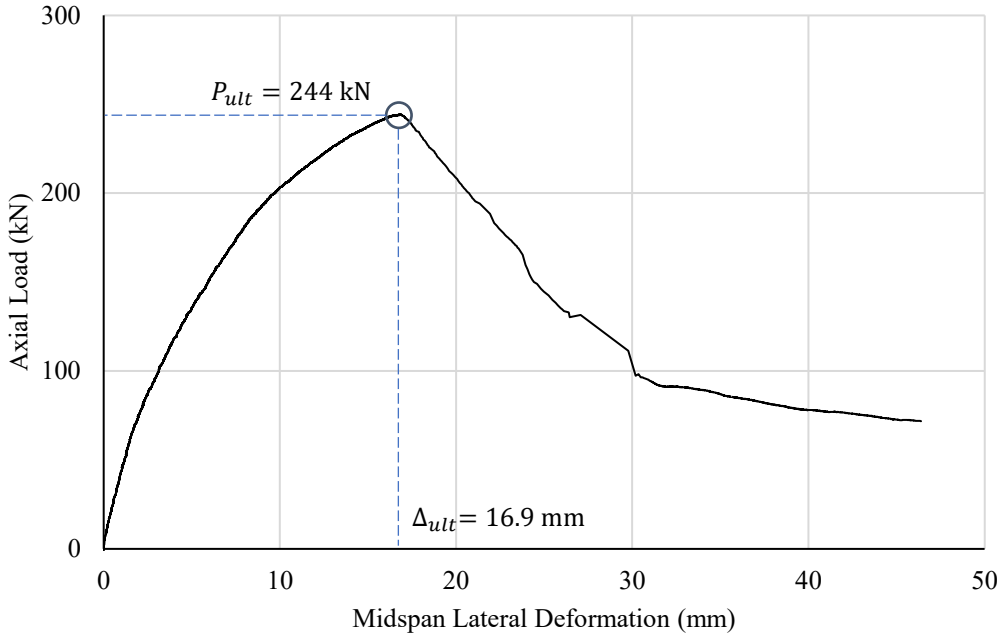

Figure 4.4. Load vs lateral deformation diagram for specimen MC.

Figure 4.5. Specimen MC after failure.

Figure 4.6. Tensile mortar joint crack openings and longitudinal compressive cracks in masonry in specimen MC.

Figure 4.7. Reinforcement local buckling in specimen MC.

This specimen was instrumented with strain gauges on the vertical reinforcement and the strain readings were then used to construct the moment-curvature relationship for this specimen. Figure 4.8 shows the moment-curvature curve for specimen MC where the moment was calculated as $P \times (e + \Delta)$ and Δ was measured at the midspan; the curvature was calculated as $(\epsilon_1 - \epsilon_2)/t$, and ϵ_1 and ϵ_2 are compressive and tensile strains measured on the reinforcement at midspan, respectively. The overall behaviour is consistent with that of load vs. deflection curve and the nonlinearity trend was similar. At failure, the moment was calculated to be M_{ult} = 18.9 kN.m with a curvature of $\epsilon_{ult} = 3.2 \times 10^{-5}$. The flexural rigidity of specimen can then be calculated using the moment-curvature relationship curve. As shown in Figure 4.8, the flexural rigidity EI_{eff}, calculated as the secant stiffness at ultimate, was 5.92×10^{11} N.mm^2. This method is commonly used in the literature and is also used for further discussions in this thesis. However, the flexural rigidity was also calculated by two other methods. One method is the secant stiffness masonry crushing strain of 0.003, and the other method is using the fundamental $M/(d^2y/dx^2)$ equation at midspan at P_{ult}. All EI_{eff} results are presented in Table 4.2

Table 4.2. Effective flexural rigidity of specimen MC by different methods.

Parameter	Method		
	Secant stiffness at P_{ult}	Secant stiffness at $\epsilon_c = 0.003$	Column deflection method $M/(d^2y/dx^2)$ at midspan at P_{ult}
Effective flexural rigidity (EI_{eff})	5.92E+11	5.10E+11	6.53E+11

Figure 4.9 shows the column lateral deflection profile along its height constructed using deflection measurements. It shows that the specimen exhibited a close to symmetrical single curvature profile with a maximum lateral deflection of 16.9 mm occurring at midspan.

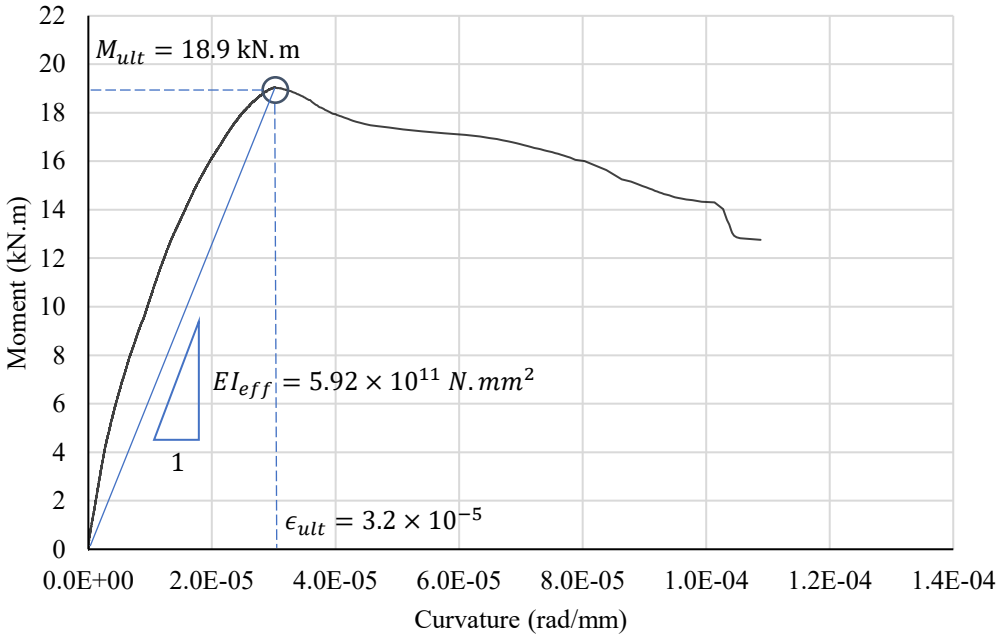

Figure 4.8. Moment vs. curvature diagram for specimen MC.

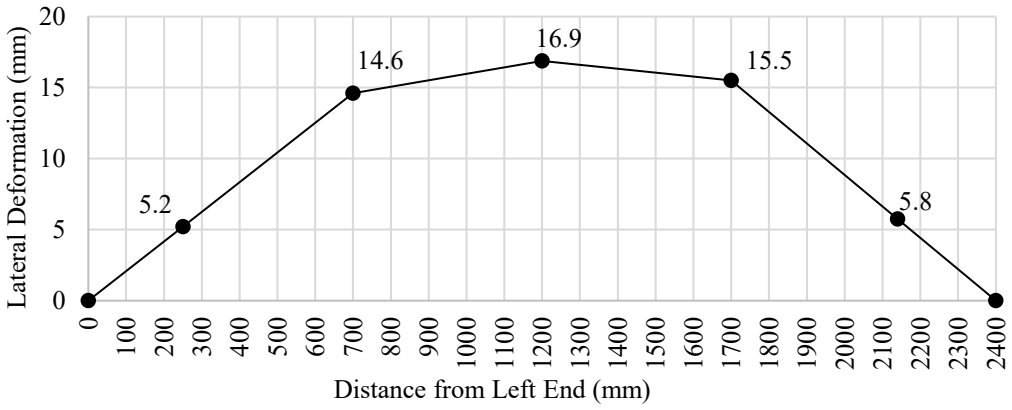

Figure 4.9. Deflection profile at the time of failure for specimen MC.

Specimen MS was tested under eccentric axial load to impose a reverse curvature loading condition. However, this test was not successful. Figure 4.10 and Figure 4.11 show the premature failure at the early stage of loading. As shown in Figure 4.11, the specimen was found to be defective as its six bottom courses were not filled with grout despite effort was made during construction to fill the cores. This created a weak section where grout was not continuous and steel reinforcement was not bonded to grout. The specimen failed suddenly at P_{ult} = 95 kN at this location while the remainder of the specimen appeared to be intact. No reverse curvature behaviour was not observed.

Figure 4.10. Specimen MS after very early pre-mature failure.

Figure 4.11. Closeup of pre-mature failed area for specimen MS.

Figure 4.12 shows the load vs. lateral deflection curves obtained at 1/4h and 3/4h points along the column height up to 95 kN. It can be observed that the deflection was greater at the defective end. The initial behaviour of both specimens was linear, but both deflections were in the same direction, indicating no reverse curvature was realized even at the outset of the loading.

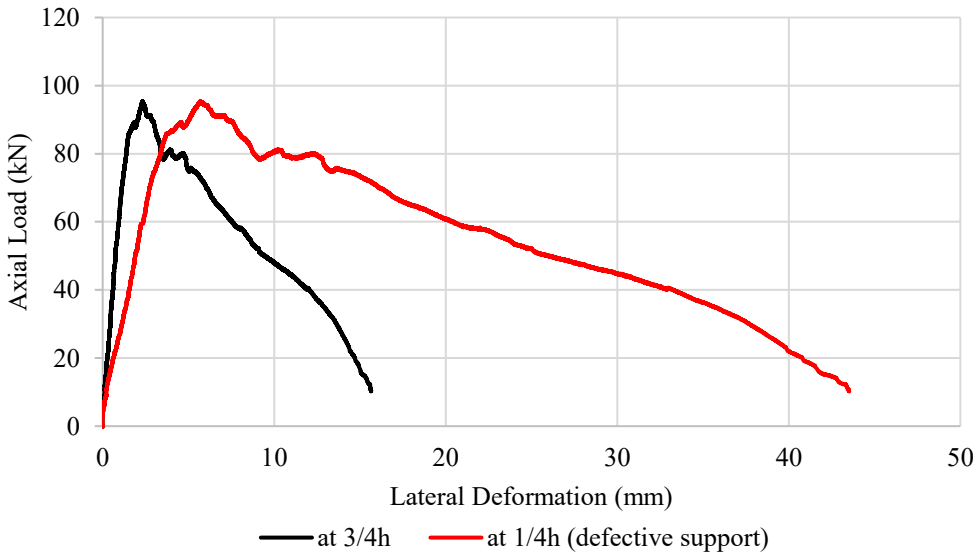

Figure 4.12. Load vs lateral deformation diagram for specimen MS.

Figure 4.13 shows the column lateral deflection profile along its height, constructed using deflection measurements. It reveals that the specimen exhibited a non-symmetrical, non-double curvature profile, with the peak lateral deflection of 2.2 mm observed near the defective support. This observation is consistent with the previous load vs. lateral deflection figure.

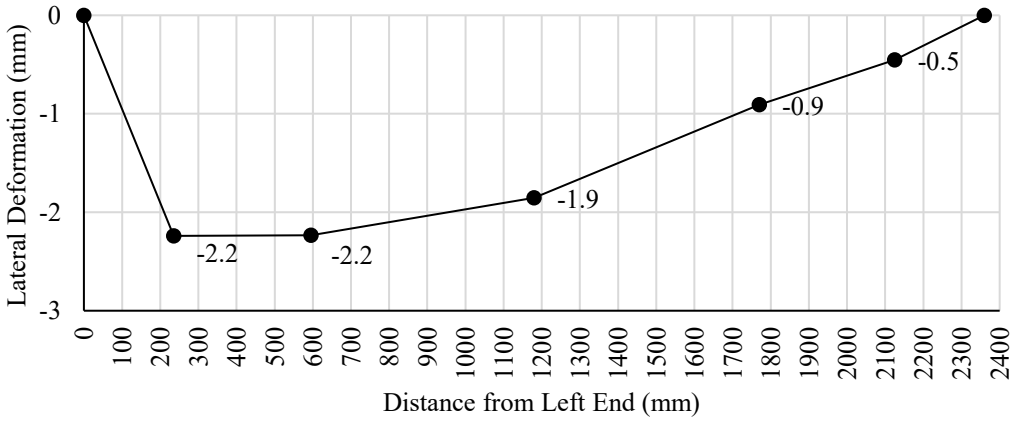

Figure 4.13. Deflection profile at the time of failure for specimen MS.

4.5 Group "T" Specimens: TS and TC

These two specimens had a height of 3000 mm (kh/t = 15.8) and were tested under eccentric axial loads with an eccentricity of 1/3t in single curvature bending. Figure 4.14 shows the comparison of axial load vs. lateral deformation curves for specimens TS and TC. Again, due to the significant difference in masonry strength (9.5 vs 19.3 MPa), specimen TC constructed with C-shaped blocks had a higher ultimate capacity when compared to specimen TS constructed with stretcher blocks. From the behaviour standpoint, the onset of nonlinearity for both specimens began immediately after loading, and the extent of this nonlinearity was more pronounced than specimen MC, indicating an increased geometric nonlinearity as the slenderness increased. Specimen TS exhibited greater deformations at ultimate load than specimen TC, indicating a more ductile behaviour. Both specimens began to show noticeable cracking around 65% of the ultimate load. As shown in the failure modes of these specimens (Figure 4.15 and Figure 4.16), damages in the form of cracking and crushing were concentrated around midspan. The tensile crack extended through the midspan mortar joints and crushing occurred on the compression side. Specimen TS failed at a load of P_{ult} of 147 kN and specimen TC failed at a load of P_{ult} of 212 kN when the longitudinal compressive reinforcement buckled on the compression side of the specimen.

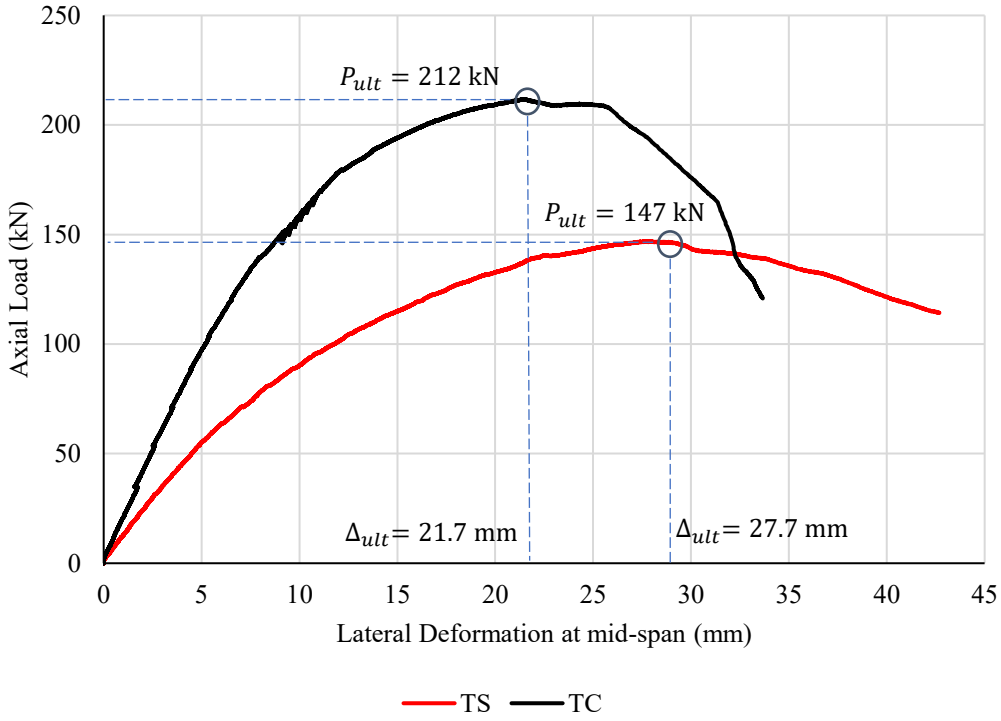

Figure 4.14. Load vs lateral deformation diagram for specimens TC and TS.

(a) specimen TC (b) specimen TS

Figure 4.15. Specimen TS and TC after failure.

(a) specimen TC (b) specimen TS

Figure 4.16. Masonry crushing and longitudinal reinforcement local buckling for specimens TC and TS.

Figure 4.17 shows the moment-curvature curves for both specimens. The overall behaviour is consistent with that of the load vs. deflection curve, and the nonlinearity trend was similar. At failure, the moment was calculated to be M_{ult} = 18.4 kN.m for specimen TC and 13.3 kN.m for specimen TS, with corresponding curvatures of $\epsilon_{ult} = 4.01 \times 10^{-5}$ and 3.12×10^{-5}, respectively. The flexural rigidity EI_{eff} was calculated to be 4.58×10^{11} N.mm^2 for specimen TC and 4.25×10^{11} N.mm^2 for specimen TS.

Figure 4.18 shows the column lateral deflection profile along their height, constructed using deflection measurements. It shows that both specimens exhibited a close to symmetrical single curvature profile with maximum lateral deflection of 21.7 mm and 27.7 mm occurring at midspan for specimens TC and TS, respectively. Table 4.3 shows EI_{eff} values calculated using all three methods. However, the secant method at ultimate load is used for further discussions in this thesis as it is the most commonly used method in the masonry literature.

Table 4.3. Effective flexural rigidity of Specimens TC and TS by different methods.

Parameter	Specimen	Method		
		Secant stiffness at P_{ult}	Secant stiffness at $\epsilon_c = 0.003$	Column deflection method $M/(d^2y/dx^2)$ at midspan at P_{ult}
Effective flexural rigidity (EI_{eff})	TC	4.58E+11	5.60E+11	7.73E+11
	TS	4.25E+11	4.40E+11	4.38E+11

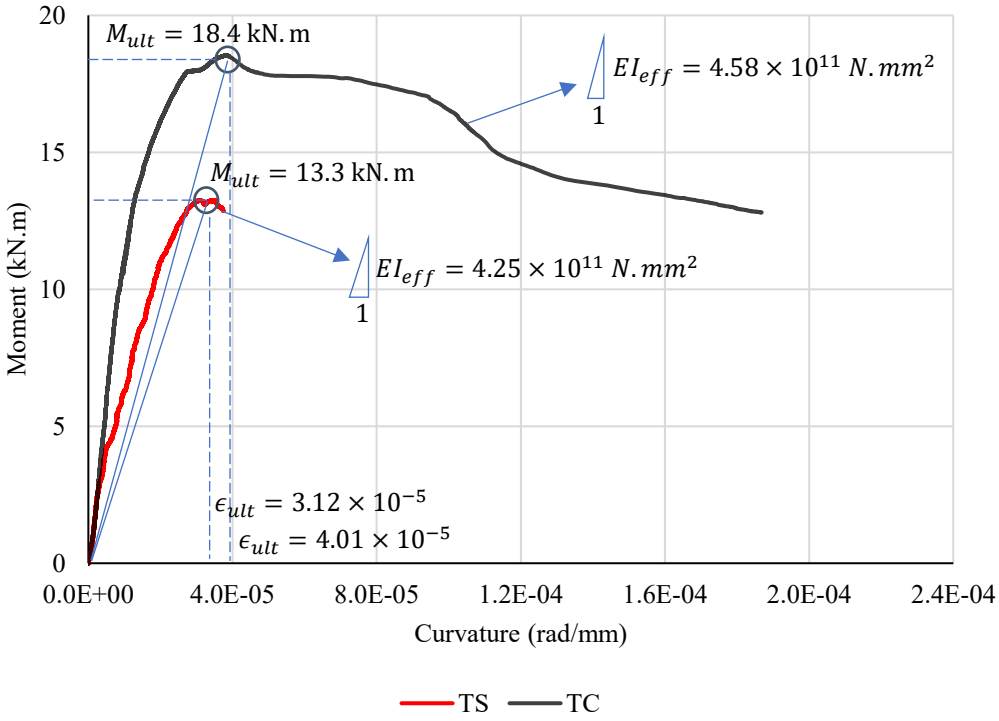

Figure 4.17. Moment vs. curvature diagram for specimens TC and TS.

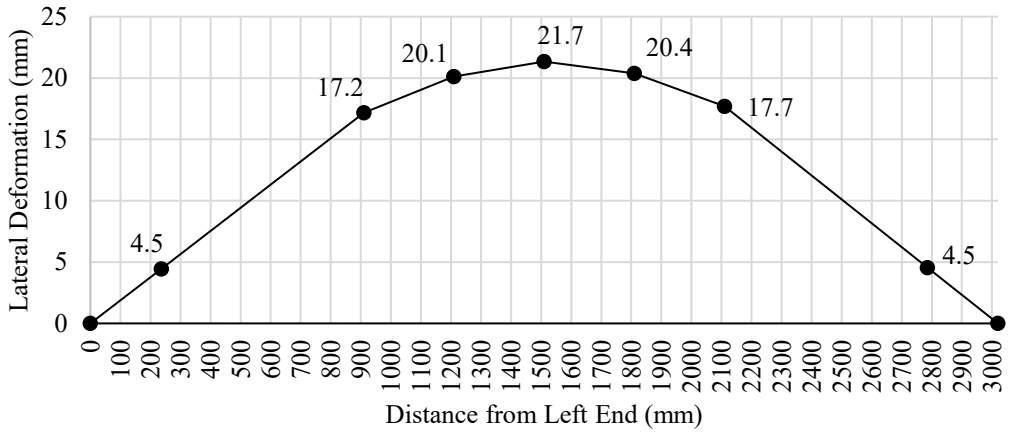

(a) specimen TC

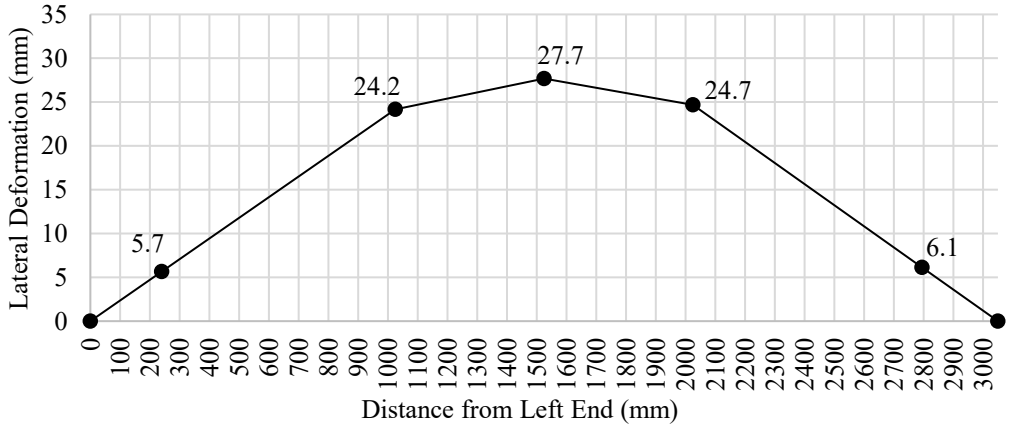

(b) specimen TS

Figure 4.18. Deflection profile at the time of failure for specimens TC and TS.

4.6 Comparison of the eccentrically loaded specimens MC and TC

Specimens MC and TC had different heights, but both were constructed with C-shaped blocks and tested under the same loading conditions. This section presents the comparison of the behaviour and failure of these two specimens to study the effect of slenderness. Figure 4.19 compares the load vs. midspan lateral deformation of these two specimens. It shows that the specimen with higher slenderness (TC), failed at a lower load but experienced greater midspan deflection. The higher slenderness specimen also showed more pronounced nonlinearity in its load vs. deflection behaviour throughout the loading history. Failure mode photos of these specimens (as seen in Figure 4.6 and Figure 4.16.a) also showed that specimen TC exhibited more extensive cracking and crushing at failure than specimen MC, which explains a more ductile failure as indicated in Figure 4.19 for specimen TC.

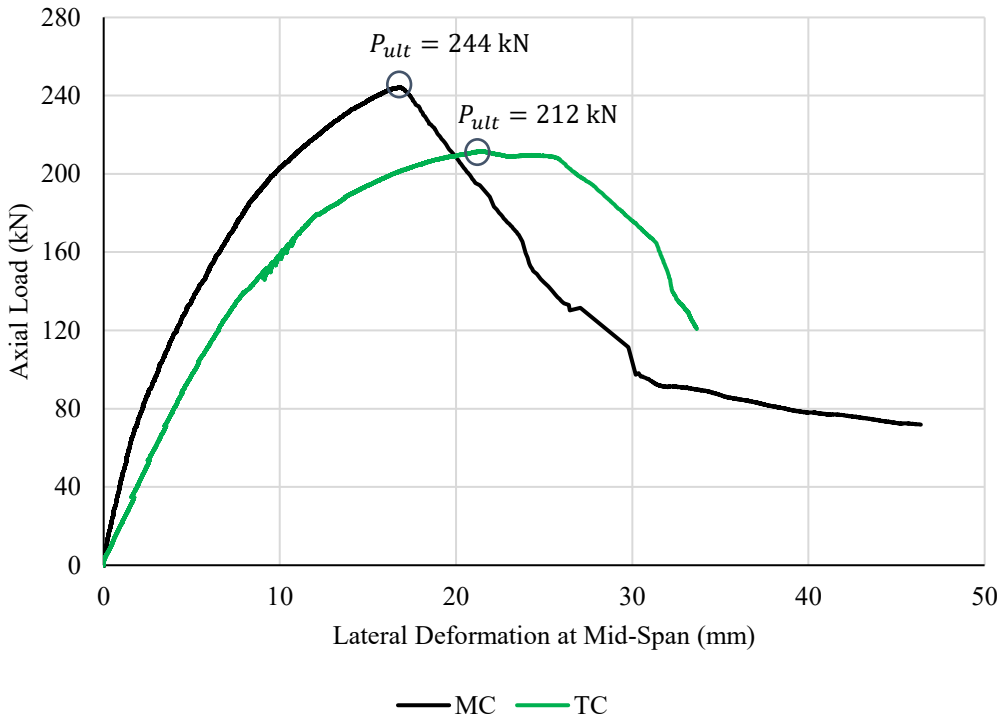

Figure 4.19. Comparison of load vs lateral deformation diagrams of eccentrically loaded specimens MC and TC.

Figure 4.20 compares the moment-curvature curves for specimens MC and TC. While the specimen with higher slenderness, TC, attained a slightly lower moment capacity at failure, the difference in the two specimens was not significant (18.4 vs. 18.9 kN.m). It is deduced that although the axial capacity of the high slenderness specimen was markedly lower, the greater midspan deflection due to a higher slenderness, contributed to a much closer failure moment for these two specimens. The EI_{eff} values calculated in the figure show that an increase in slenderness from kh/t = 12.6 to 15.8 resulted in a decrease in EI_{eff} of 22 percent. The high slenderness specimen attained a greater curvature at failure, and this, combined with a lower moment, resulted in a lower flexural rigidity.

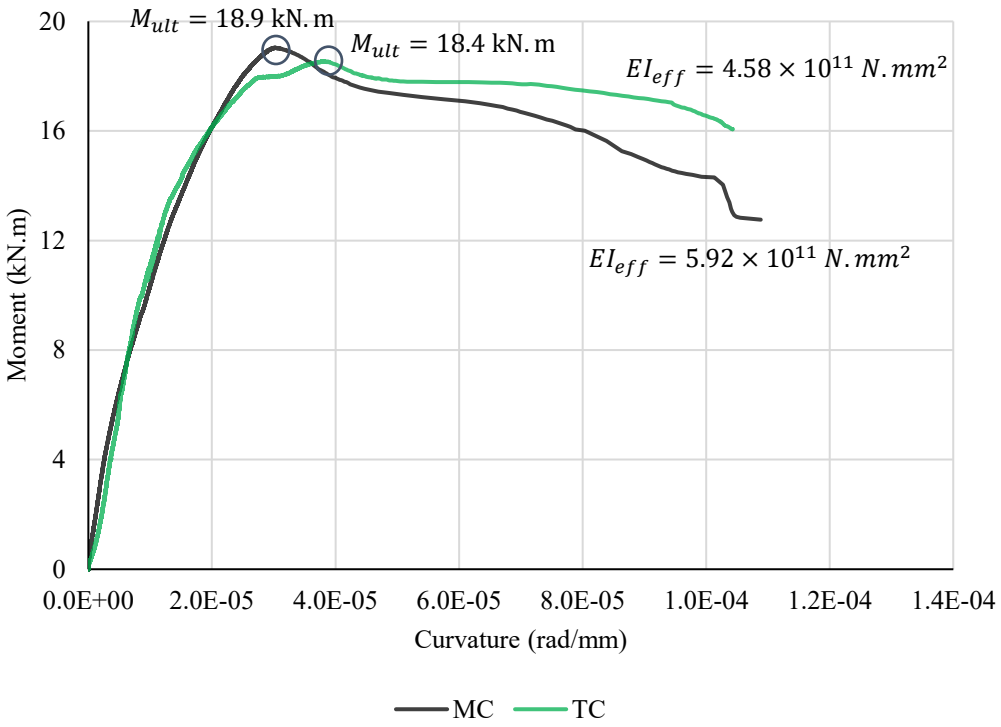

Figure 4.20. Comparison of moment-curvature diagrams of eccentrically loaded specimens, MC and TC.

4.7 Comparison of test results with CSA S304 and TMS 402

Table 4.4 shows the comparison of P_{ult}, M_{ult}, and EI_{eff} values obtained from experimental test results, CSA S304, and TMS 402/602. The calculation of these values from test results was explained in the previous sub-chapters. To obtain the code values based on CSA S304 and TMS 402/602, the equations presented in Chapter 2 were used. Sample calculations of based on the CSA S304 and TMS 402/602 are presented in Appendix B.

Table 4.4. Comparison of test results with code values.

Specimen ID	f'_m (MPa)	P_{ult} (kN)			M_{ult} (kN.m)			EI_{eff} (N.mm^2) $\times 10^{11}$		
		Test	CSA	TMS	Test	CSA	TMS	Test	CSA	TMS
SC	18.5	675	714	681	-	-	-	-	-	-
SS	8.5	468	396	382	-	-	-	-	-	-
MC	20.5	244	185	243	18.9	18.1	17.5	5.92	4.58	11.6
TC	19.3	212	138	212	18.4	15.7	16.7	4.58	4.32	9.99
TS	9.5	147	99	133	13.3	10.4	10.3	4.25	3.52	6.91

Both codes show a decreasing trend of P_{ult} values with an increase in slenderness. For all specimens except specimen SC, the ultimate axial loads, P_{ult}, predicted by CSA S304 and TMS 402/602 are lower than the experimental results, but the degree of underestimation exhibited by the two codes are markedly different. While CSA S304 underestimates P_{ult} by an average of 30.6 percent, the TMS 402/602 P_{ult} values were much closer to the test results, especially for eccentrically loaded columns. In all three presented cases, the TMS 402/602 values were almost identical to the test results. In terms of M_{ult} values, the test results were calculated as $P_{ult} \times (e + \Delta_{ult})$ whereas the two code values were the total moment under the

respective P_{ult} values using the respective moment magnifier equations. The fact that the two code P_{ult} values were markedly different while their M_{ult} values were close suggests that the moment magnifier would be markedly different. This is demonstrated through the comparison of values of effective flexural rigidity, EI_{eff}. The CSA S304 method underestimated EI_{eff} of eccentrically loaded specimens by an average of 15 percent but the TMS 402/602 method produced much greater EI_{eff} values which were, on average, 1.9 times the experimental results. Referring to the sample calculation presented in Appendix B, this significant difference in EI_{eff} values is attributed to the fact that the compressive load was included in the calculation by TMS 402/602. Interestingly, while the TMS EI_{eff} values resulted in estimated P values close to the experimental results, they are different from the experimentally determined EI_{eff} values. Since the experimental EI_{eff} values were obtained at the midheight of the column, this may suggest that applying the EI_{eff} at one point along the column height to represent the flexural rigidity of the entire column might be problematic in the moment magnifier method.

To obtain P_{ult} and M_{ult} based on these codes, the intersection of the magnified e = t/3 curve with the specimen P-M interaction diagram is used. Figure 4.21, Figure 4.22, and Figure 4.23 show the load vs. moment curves plotted on P-M interaction diagrams for specimens TC, TS, and MC, respectively. First, the P-M interaction diagrams for these specimens were constructed based on their geometry, reinforcement situation, and material properties. The green curves in the diagrams represent the experimental load vs. moment curves. The other two curves represent the P vs. M relationship for an eccentricity of 1/3t incorporating the moment magnification effect using the code values. When comparing the test results

(green curve), these figures indicate that TMS 402/602 provides a more realistic set of moment magnification factors than CSA S304.

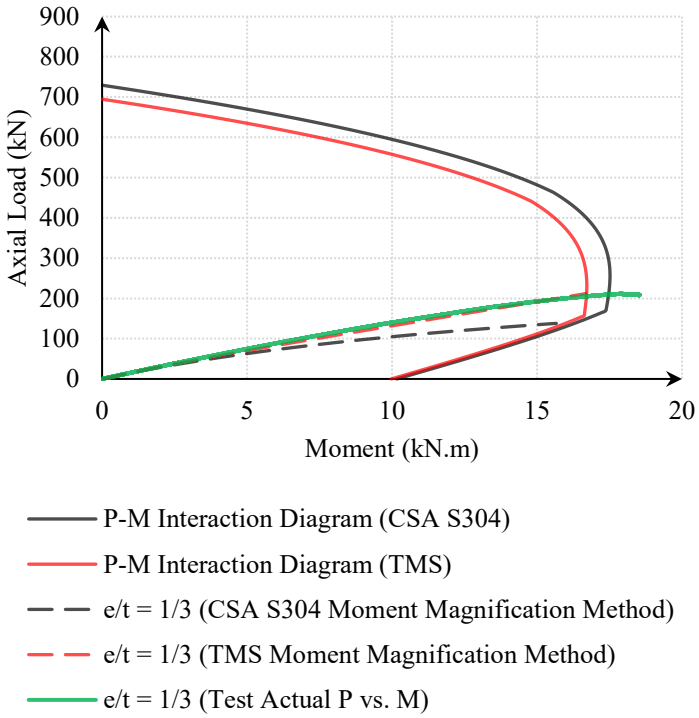

Figure 4.21. P vs. M using CSA S304, TMS 402/602, and Test Result (Specimen TC).

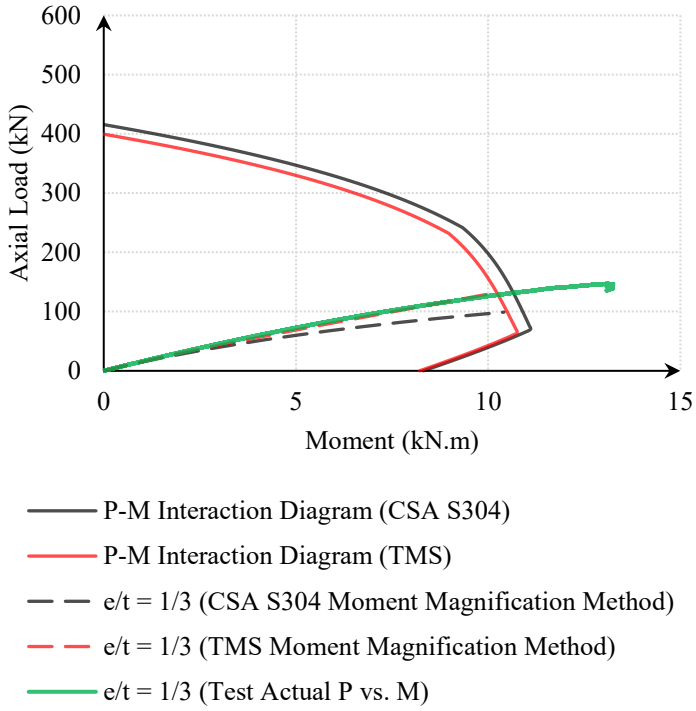

Figure 4.22. P vs. M using CSA S304, TMS 402/602, and Test Result (Specimen TS).

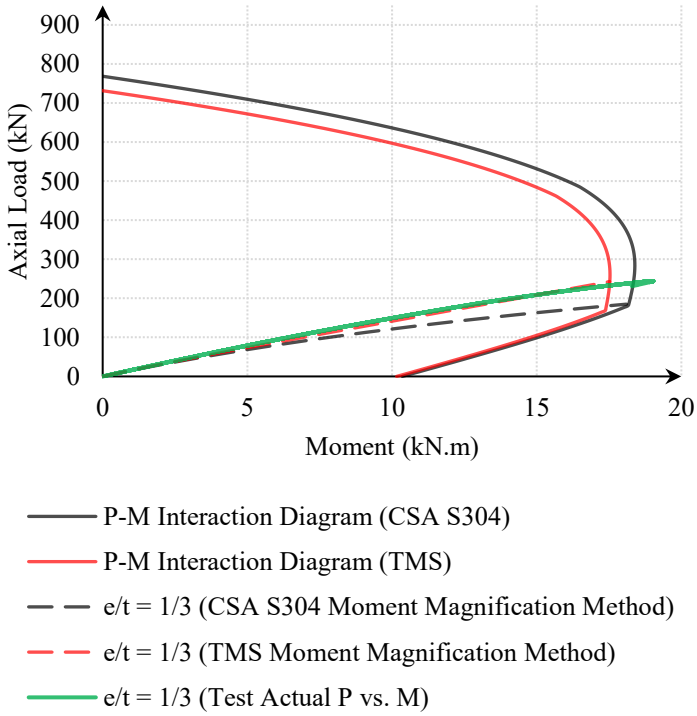

Figure 4.23. P vs. M using CSA S304, TMS 402/602, and Test Result (Specimen MC).

Chapter 5 Numerical Modeling and Verification

5.1 Introduction

This chapter describes the finite element (FE) model developed in this study to investigate the behaviour of masonry columns under the combined influence of axial load and bending moment. The methodology in the development of the FE model using the SAP2000 software package and its validation using the test results are presented in the following sections.

5.2 Methodology

Six numerical models were constructed using the SAP2000 finite element software. SAP2000 was selected due its capability of nonlinear 3D finite element modeling at low computational cost. The fiber element nonlinear modeling technique was adopted for simulating column specimens within the SAP2000 software. In this approach, column cross-sections were meshed using fober element, and material behaviour models were assigned to each element in the cross-section based on the model proposed by Priestley & Elder (1983).

5.2.1 General Model Properties

Figure 5.1 displays the properties of a typical masonry column model created in SAP2000. A "Frame Element" is employed to define the column within the SAP2000 environment. The cross-section of this frame element mirrors the dimensions of the actual column specimens constructed in the laboratory. The eccentricity of the end support is simulated

by incorporating a rigid beam element between the end node at the centerline and an eccentric joint located on the same cross-section but with the appropriate offset. These offset joints are constrained against translation in all spatial directions and rotation about the lateral axis. One of the ends is also restrained against torsion to ensure stability. Displacement controlled loading is applied at the right end of the specimen to match the loading conditions in the test. Nonlinear direct integration time history analysis was used with consideration of geometric nonlinearity to account for the second order effects ($P-\Delta$).

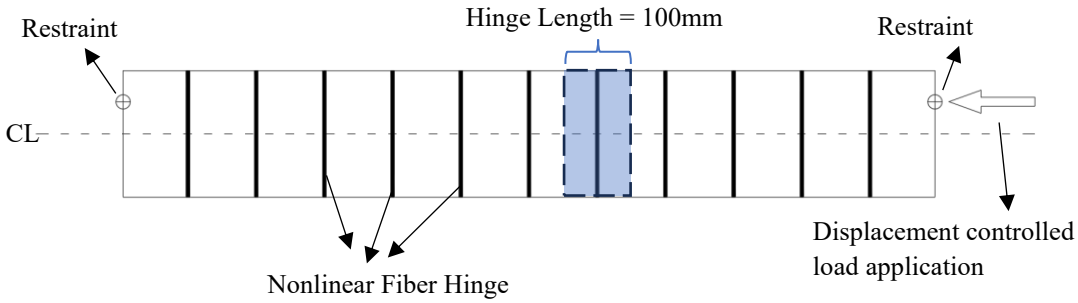

Figure 5.1. Typical properties of the numerical SAP2000 model.

Fiber hinges, each measuring 100 millimeters in length, are designated to the frame element at regular intervals of 100 millimeters along its length, ensuring that nonlinearity is captured throughout the entirety of the column. Figure 5.2 exhibits a representative cross-section of a fiber hinge.

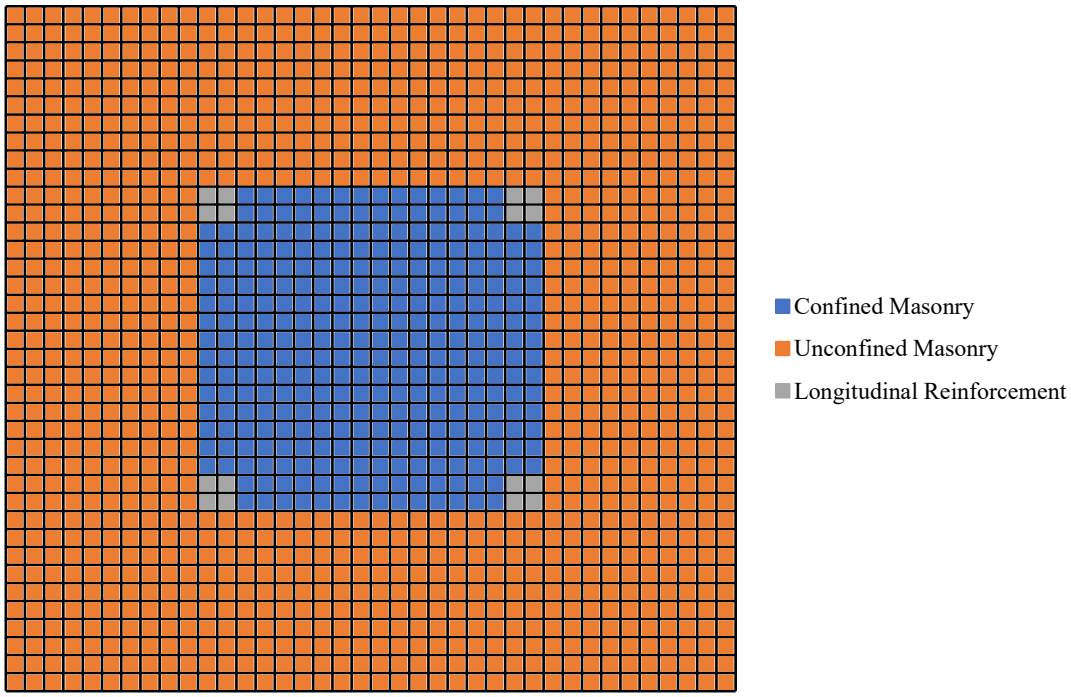

Figure 5.2. A typical meshed fiber hinge cross section in the numerical SAP2000 model.

5.2.2 Nonlinear behaviour of masonry and reinforcement materials

The behaviour of grout, block, and mortar is modeled as a continuum using the Priestley & Elder (1983) stress-strain relationships. The unconfined stress-strain relationship adopts a rising parabolic curve (Eqn. 5.1), transitioning to a declining linear failure line (Eqn. 5.2), concluding with a horizontal plateau following the intersection of this falling linear branch with the strain axis.

$$f_m = 1.067 f_m^{'} \left[\frac{2\varepsilon_m}{0.002} - \left(\frac{\varepsilon_m}{0.002} \right)^2 \right] \qquad for\ \varepsilon_m \le 0.0015 \tag{5.1}$$

$$f_m = f_m^{'} \left(1 - Z_m \left(\varepsilon_m - 0.0015 \right) \right) \qquad for\ \varepsilon_m > 0.0015 \tag{5.2}$$

where

$$Z_m = \frac{0.5}{\frac{3+0.29f_m^{'}}{145f_m^{'}-1000} - 0.002} \tag{5.3}$$

The confined stress-strain relationship features a rising parabolic curve (Eqn. 5.4), succeeded by a declining linear failure line (Eqn. 5.6). It culminates in a horizontal plateau when the stress approximates $0.2f_m'$.

$$f_m = 1.067Kf_m^{'}\left[\frac{2\varepsilon_m}{0.002K} - \left(\frac{\varepsilon_m}{0.002K}\right)^2\right] \qquad for\ \varepsilon_m \le 0.002K \tag{5.4}$$

where

$$K = 1 + \left(\frac{\rho_s f_{yh}}{f_m^{'}}\right) \tag{5.5}$$

$$f_m = Kf_m^{'}\left[1 - Z_m(\varepsilon_m - 0.002K)\right] \qquad for\ \varepsilon_m > 0.002K \tag{5.6}$$

where

$$Z_m = \frac{0.5}{\frac{3+0.29f_m^{'}}{145f_m^{'}-1000} + \frac{3}{4}\rho_s\sqrt{\frac{h^{"}}{s_h}} - 0.002K} \tag{5.7}$$

where f_m = compressive stress on the vertical axis of stress-strain relationship; f_m' = specified compressive stress of masonry; f_{yh} = Tensile strengths of ties; ϵ_m = compressive strain on the horizontal axis of stress-strain relationship; h'' = dimension of the confined

grouted core in the cross-section; s_h = spacing of the ties; and Z_m = slope of the stress-strain curve's linear post peak branch.

Figure 5.3 illustrates a typical stress-strain curve for both confined and unconfined masonry with a strength of f'_m = 9.1 MPa. These curves are attributed to the confined and unconfined elements within the fiber hinge cross-section.

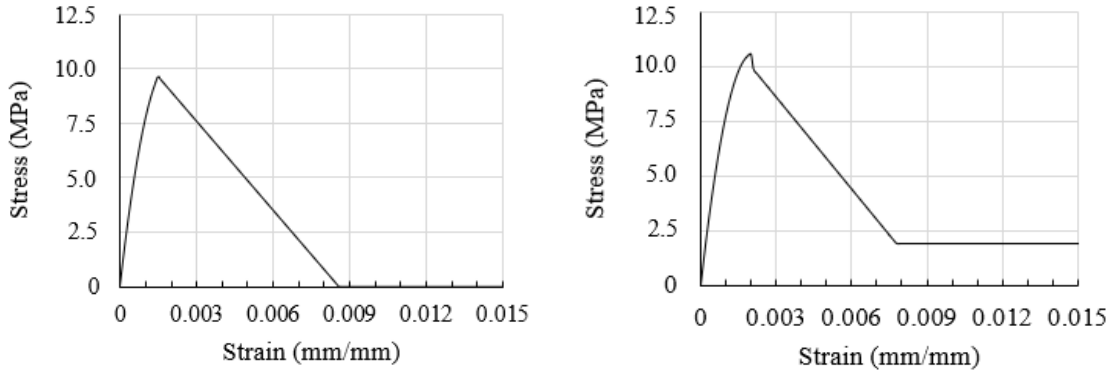

(a) unconfined (b) confined

Figure 5.3. A typical compressive behaviour of unconfined (a) and confined(b) masonry.

The stress-strain relationship for the longitudinal reinforcement is derived from auxiliary test results on rebar specimens. Since the longitudinal reinforcement was tied in accordance with the CSA S304 standards, the compressive branch of the stress-strain curve mirrors the tensile branch, but with an opposite sign. Figure 5.4 presents a typical stress-strain curve for the steel meshes within the fiber hinge.

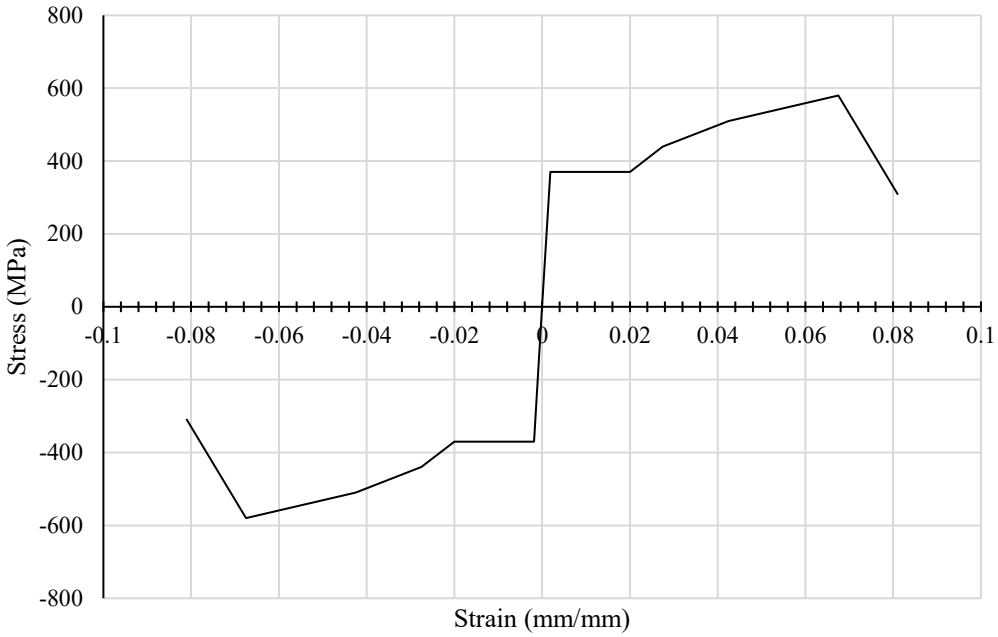

Figure 5.4. A typical behaviour of longitudinal reinforcement under tension and compression.

5.3 Numerical Model Results and Verification

5.3.1 Specimens SC and SS

Figure 5.5 and Figure 5.6 show the comparison of numerical and experimental load vs. axial deformation curves for specimens Sc and SS. Overall, the results from the numerical models compare well with the experimental data in both stiffness and ultimate capacity. A slightly greater discrepancy in capacity observed in specimen SC (678 vs. 784 kN) was attributed to a probable construction defect in the specimen as the specimens showed an abrupt reduction in load around 600 kN.

Figure 5.7 illustrates the comparison of numerical and experimental load vs. axial strain curves for these two specimens. The experimental axial strains were average strains obtained from strain readings on two longitudinal reinforcement on either side of the cross-section. It can be seen that the model is capable of predicting strains with reasonable accuracy.

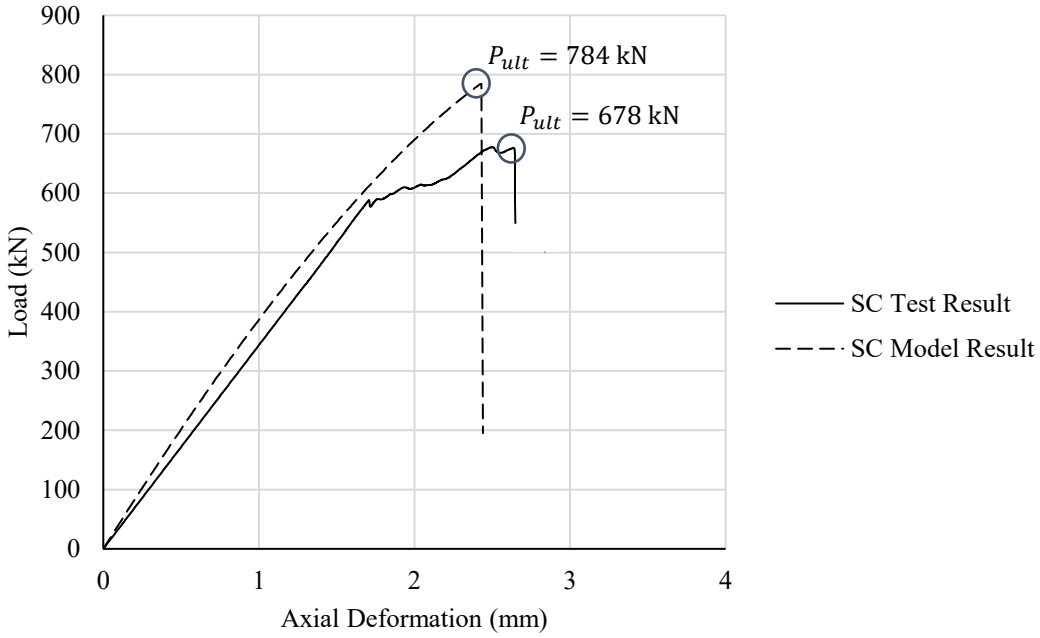

Figure 5.5. Comparison of specimen SC test versus numerical model results.

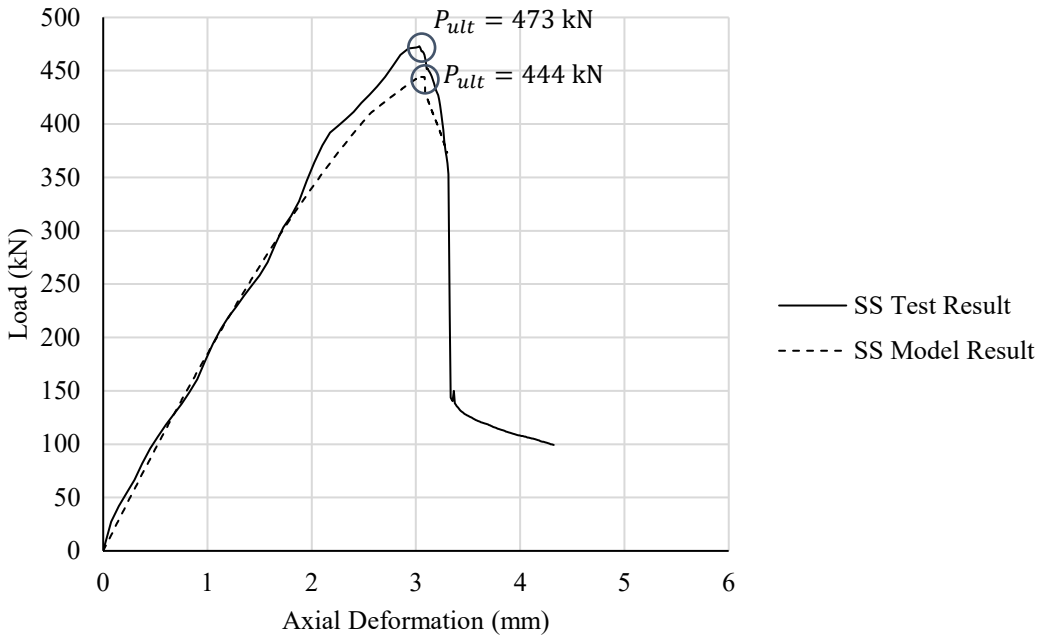

Figure 5.6. Comparison of specimen SS test versus numerical model results.

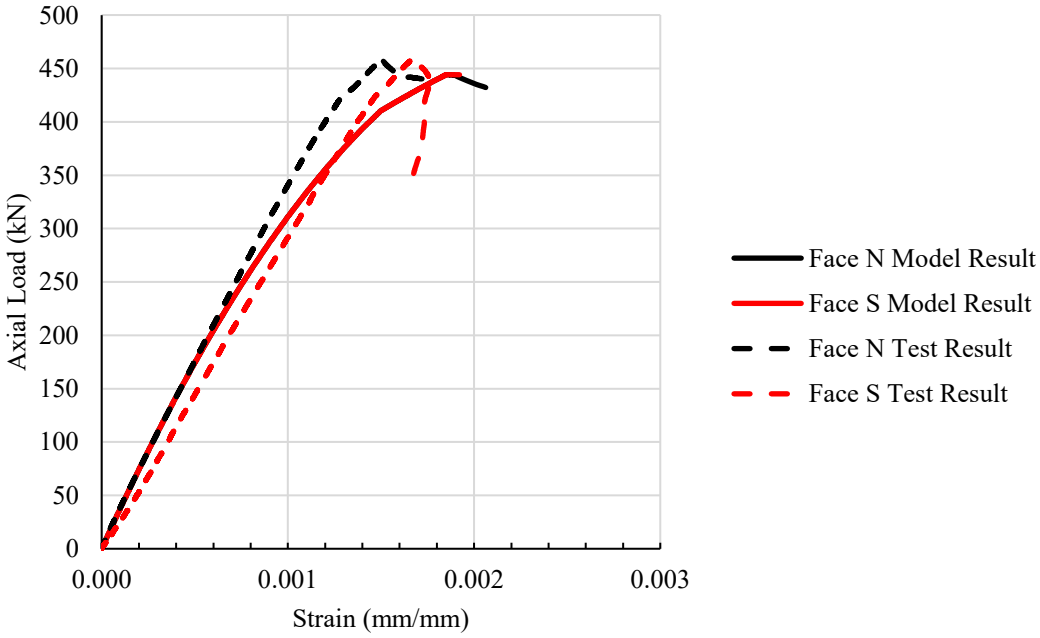

Figure 5.7. Comparison of load vs.strain curves for specimen SS.

5.3.2 Spceimens MC, TC, and TS

Figure 5.8 compares the moment-curvature relationship and Figure 5.9 compares the load vs. lateral deflection curves for specimens MC, TC and TS. Both figures show a good performance of the numerical model in capturing the behaviour and capacity of eccentrically loaded specimens. It is noted that in the load vs. lateral deflection comparison, the numerical model showed a lower stiffness than the test results up to the ultimate load. The post-ultimate behaviour capture still remained challenging.

Figure 5.10 illustrated the comparison of load vs. axial strain curves for specimens MC, TC, and TS. Again, the model is capable of predicting the trend and value with reasonable accuracy.

Figure 5.11 compares the deformation profiles of specimens MC, TC, and TS at peak axial load. Again, the model is proven to be capable of predicting the behaviour of reinforced masonry columns reasonably accurate.

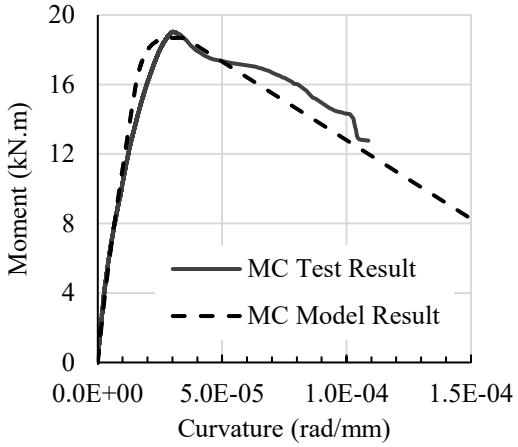

(a) specimen MC

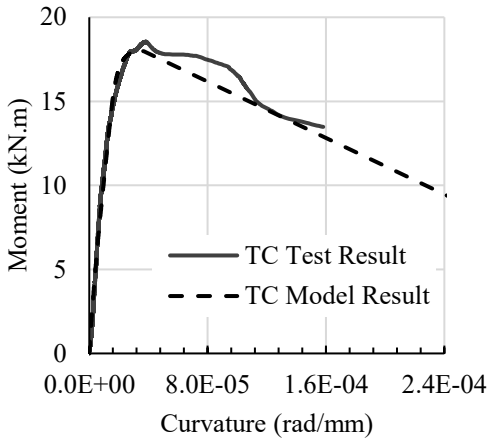

(b) specimen TC

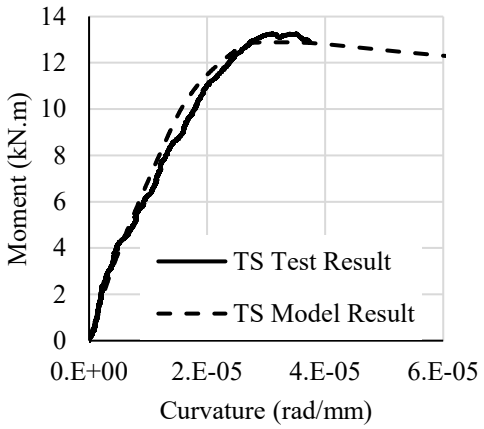

(c) Specimen TS

Figure 5.8. Comparison of moment-curvature results for specimens MC, TC, and TS.

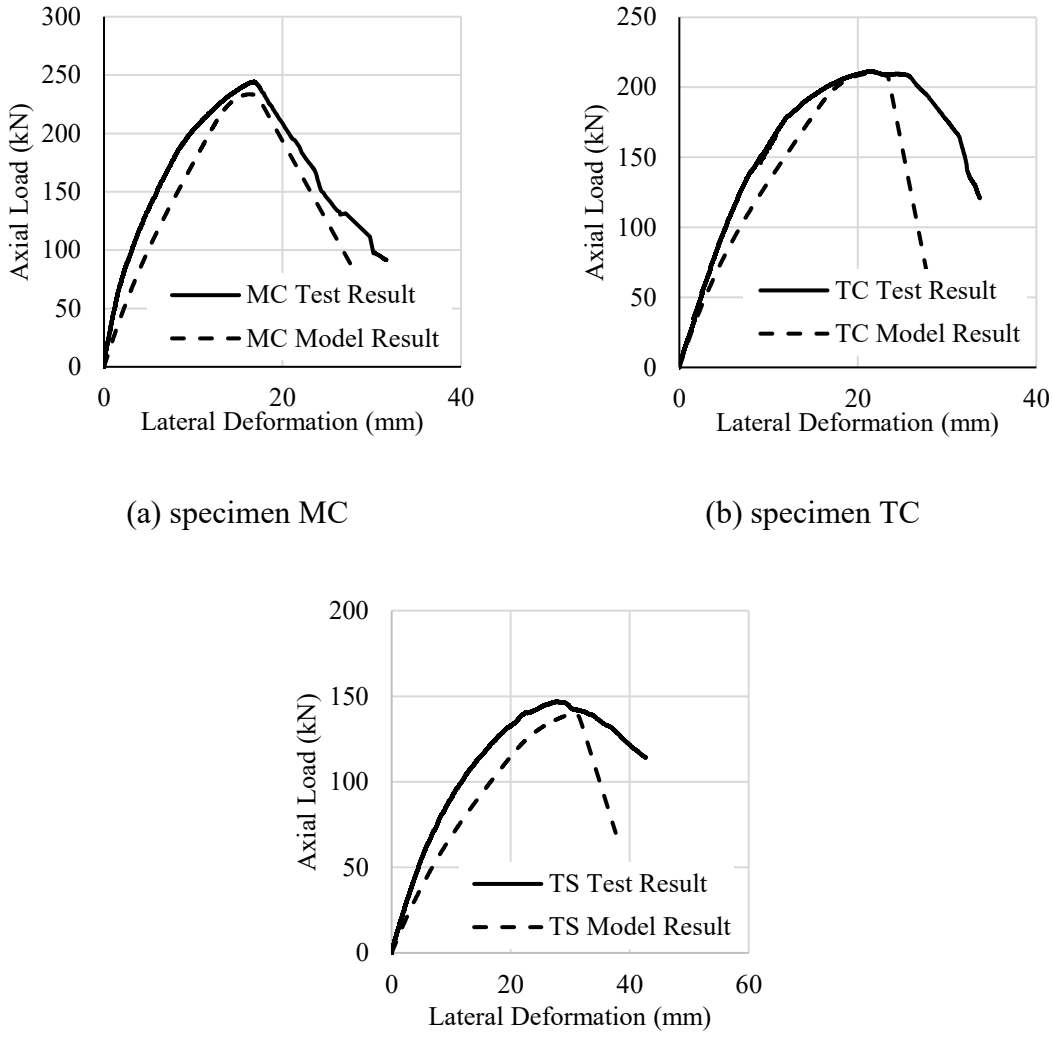

(a) specimen MC

(b) specimen TC

(c) Specimen TS

Figure 5.9. Comparison of load vs. lateral deflection curves for specimens MC, TC, and TS.

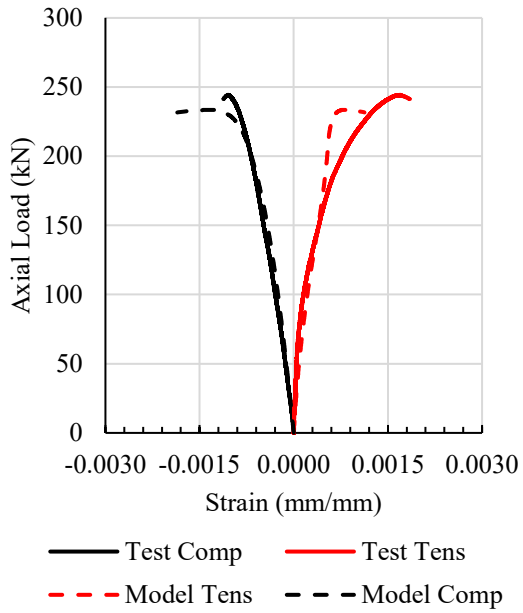

(a) specimen MC

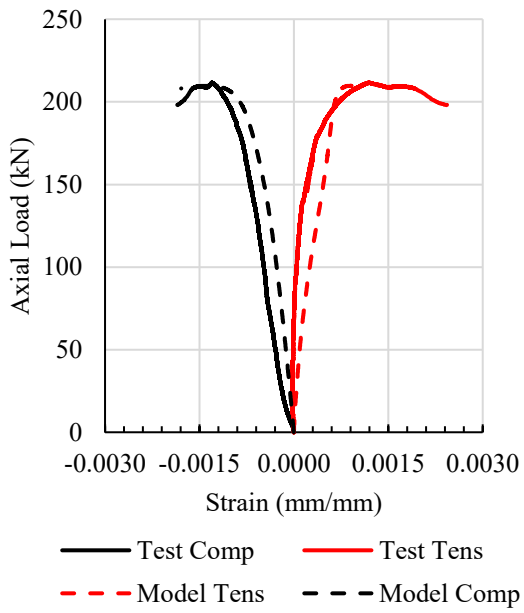

(b) specimen TC

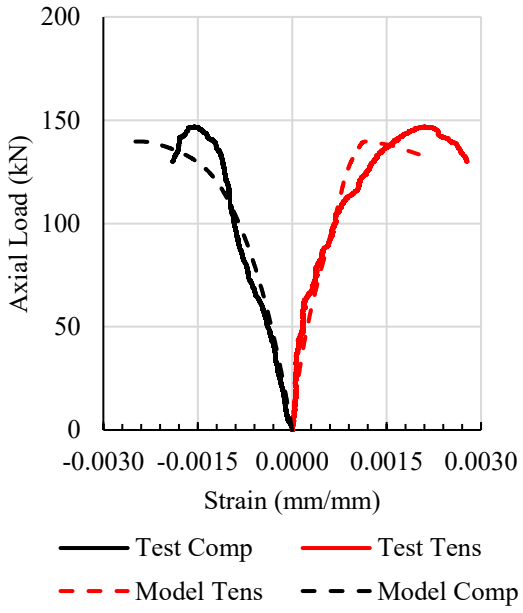

(c) Specimen TS

Figure 5.10. Comparison of load vs. axial strain curves for specimens MC, TC, and TS.

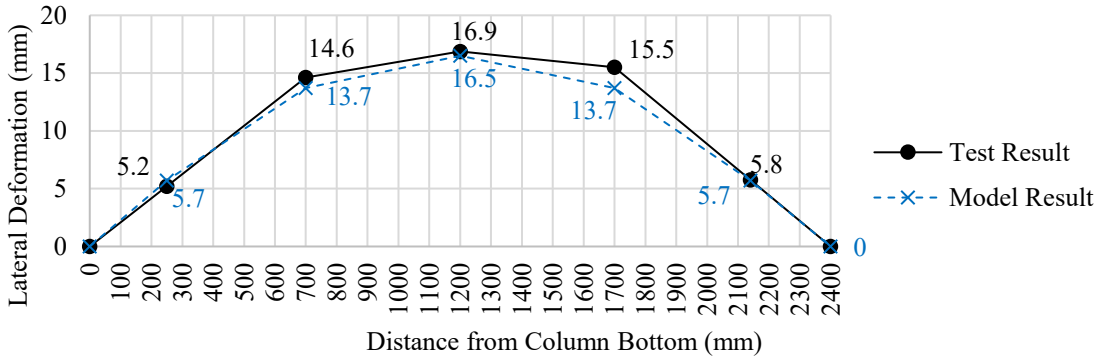

(a) Specimen MC

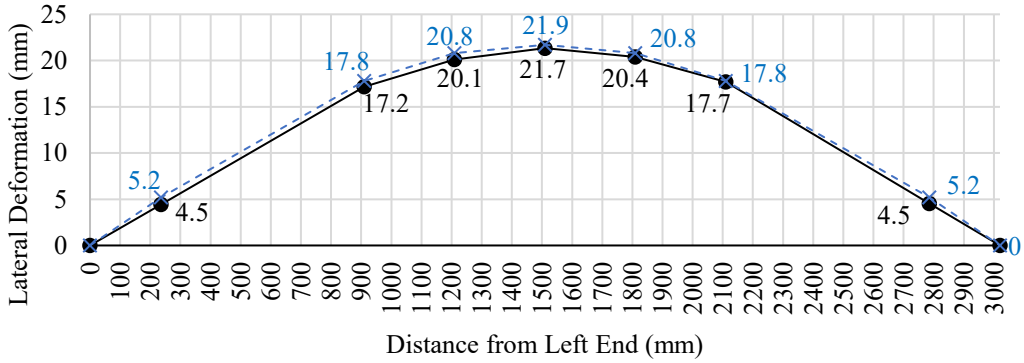

(b) Specimen TC

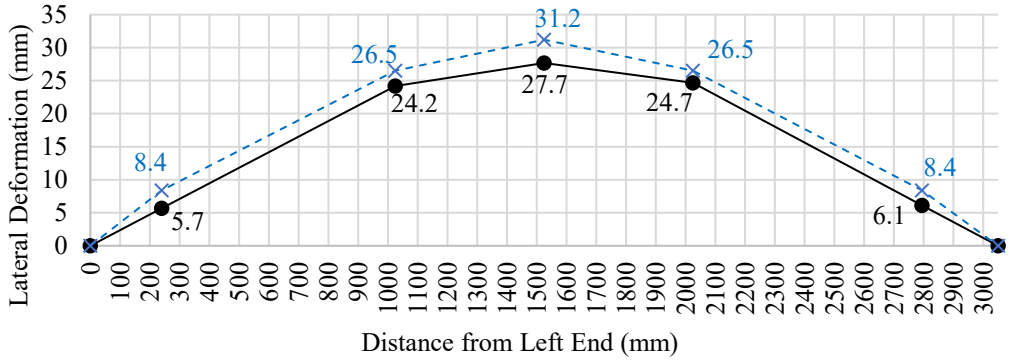

(c) Specimen TC

Figure 5.11. Comparison of deformation profiles for specimens MC, TC, and TS.

5.4 Summary

Overall, the numerical model developed in this study is shown to be capable of predicting with reasonable accuracy in the stiffness, deformation, deflection, and capacity of both concentrically and eccentrically loaded masonry columns. While more detailed validation on more specimens is needed to further confirm the performance of the model, this study showed that the use of the Priestley and Elder material model with the fiber hinge element modeling technique in SAP2000 can provide a satisfactory and efficient FE model for analysis of masonry columns.

Chapter 6 Parametric Study

6.1 Introduction

A parametric study, focusing on the effect of slenderness ratio (kh/t) and axial load eccentricity (e) was conducted. the results are presented in this chapter. The numerical model described in Chapter 5 was used in this parametric study.

6.2 Specimen Matrix

In this parametric study, effective slenderness ratios of 6, 12, 16, 23, and 31 were considered to account for low, medium, and high (above the 30 limit) slenderness ratios. For each slenderness, eccentricity values of 0, t/6, t/3, and t/2 were considered to represent a full range of eccentricities that will place the column cross-section in full compression to partially tension. This matrix resulted in a total of 20 FE models. The cross-sectional dimensions and reinforcement as in the experimental specimens were consistently used for this study. For FE models, the masonry strength used was 9.1 MPa.

6.3 Results and Discussion

6.3.1 Effect of Effective Slenderness (kh/t)

Figure 6.1 illustrates the comparison of load vs. lateral deflection diagrams of specimens with varying kh/t for each e/t ratio. As evident from the diagrams, the degree of nonlinearity increases and the axial load-bearing capacity decreases with an increase in slenderness. This is consistent for all eccentricities.

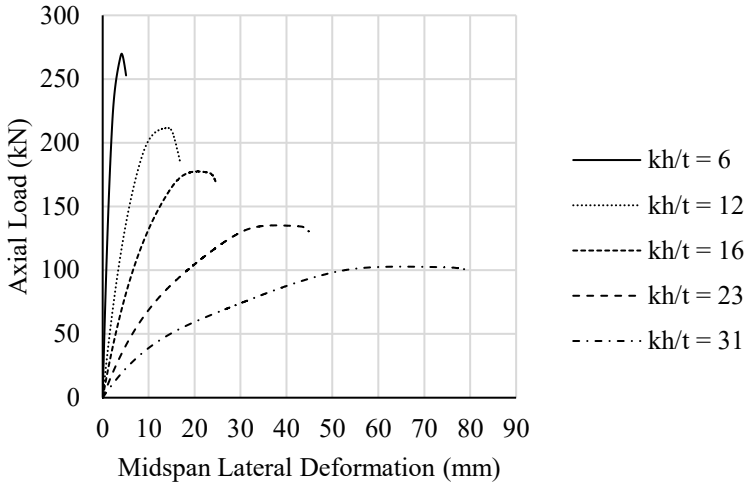

(a) e = t/6

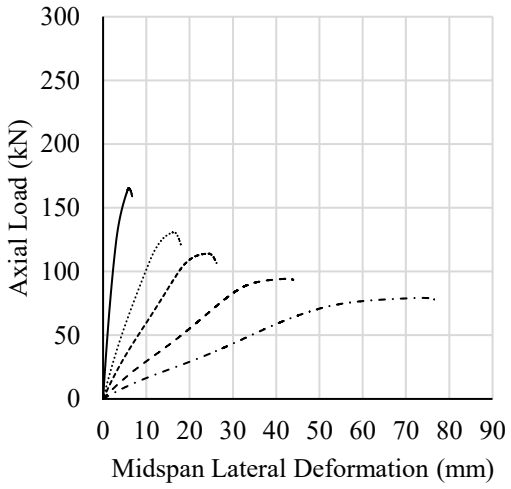

(b) e = t/3

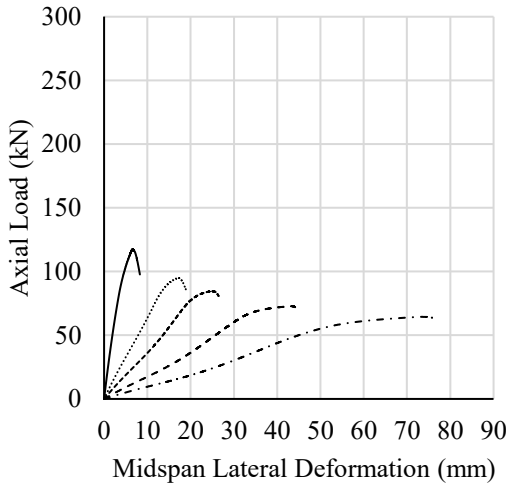

(c) e = t/2

Figure 6.1. Axial load vs. midspan lateral deformation with respect to kh/t.

Figure 6.2 shows the axial load capacity vs. slenderness ratio for all FE specimens together with predictions from CSA S304 and TMS 402/602. For specimens with kh/t = 31, the cap

limit for specimens specified by CSA S304 was also included in the figure as an empty circle.

The figure shows that as the slenderness increases, all three sources of results indicate a decreasing trend of compressive capacity. However, when compared with numerical results, the performances of CSA S304 and TMS 402/602 deviates markedly. Overall, CSA S304 tends to underestimate the compressive capacity of reinforced masonry columns and the degree of this underestimation increases as the column slenderness increases. This observation is consistent for all eccentricities, however, the smaller the eccentricity, the more pronounced this phenomenon. On the other hand, TMS 402/602 shows overestimation for column capacity for small eccentricity (e/t=1/6) but reasonably accurate predictions for other eccentricities. For specimens with a kh/t of 31, the numerical axial load capacity exceeds the cap value (10% of the capacity of concentrically loaded columns) specified by CSA S304 for very slender columns.

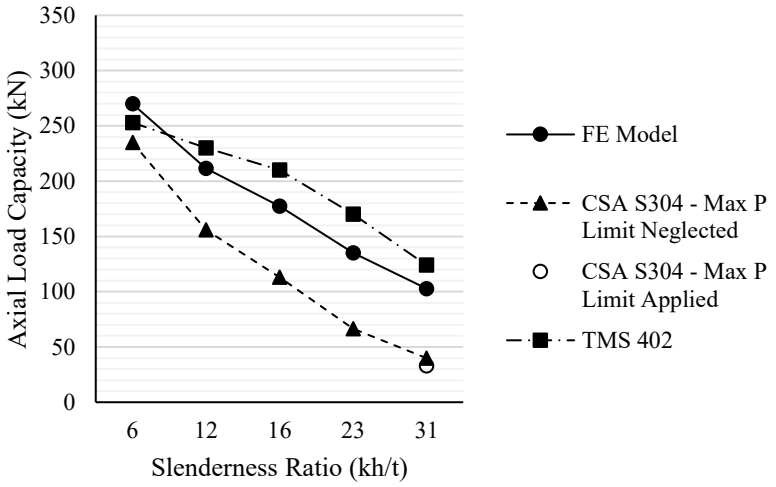

(a) e = t/6

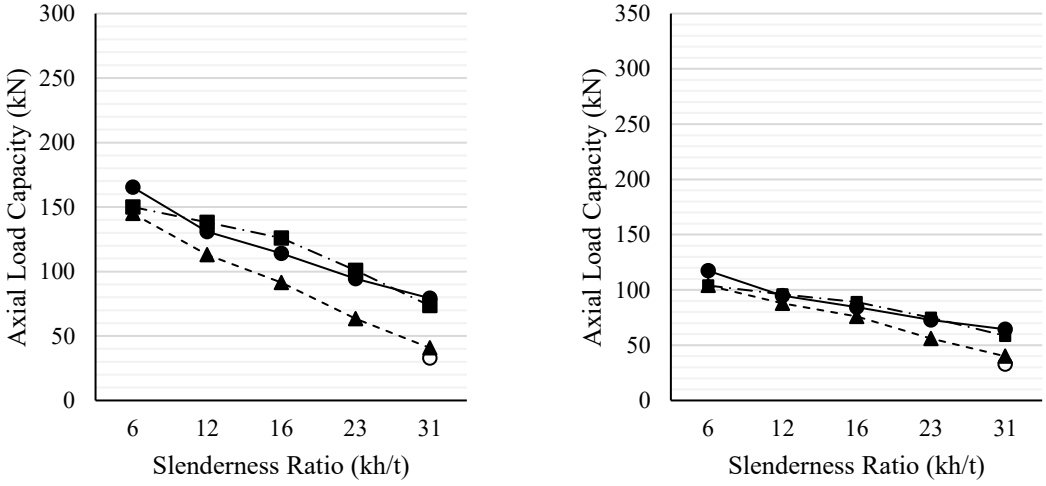

(b) e = t/3

(c) e = t/2

Figure 6.2. Axial load capacity vs. effective slenderness with respect to kh/t.

6.3.2 Effect of Eccentricity (e)

Using the results presented in Figure 6.1, the effect of eccentricity is demonstrated in Figure 6.3 where the numerical axial load vs. eccentricity ratio curves are plotted along with CSA S304 and TMS 402/602 values for each slenderness. Again, the most pronounced discrepancy between the numerical and S304 values is observed at the low eccentricity and high slenderness. In the extreme case when e/t=1/6 and kh/t=31, the underestimation by CSA S304 is approximately 50 percent. As the eccentricity increases, the agreement between the numerical axial capacity and the S304 suggested values increases. The overall performance of TMS 402/602 results is comparably better with most predictions close to the numerical values.

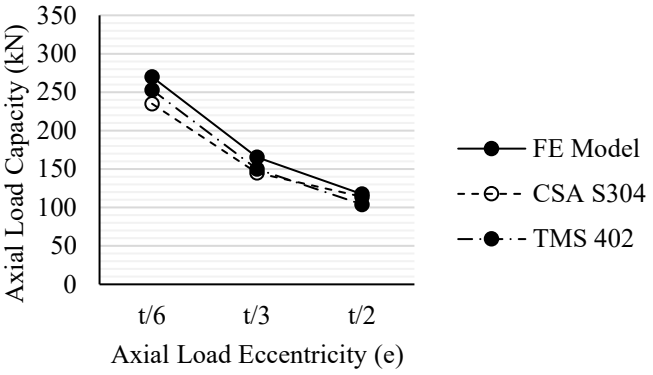

(a) kh/t = 6

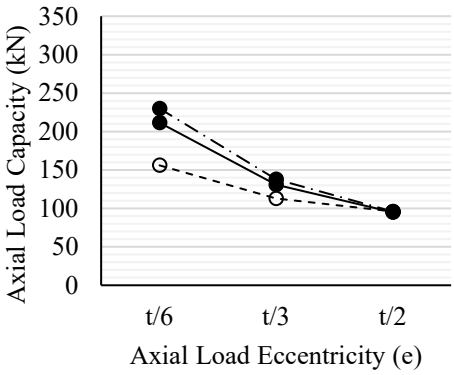

(b) kh/t = 12

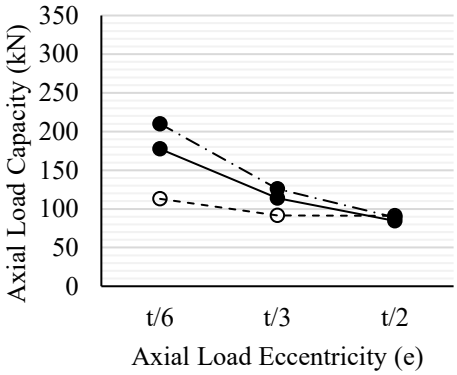

(c) kh/t = 16

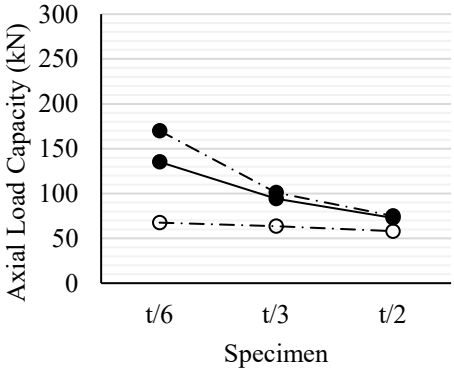

(d) kh/t = 23

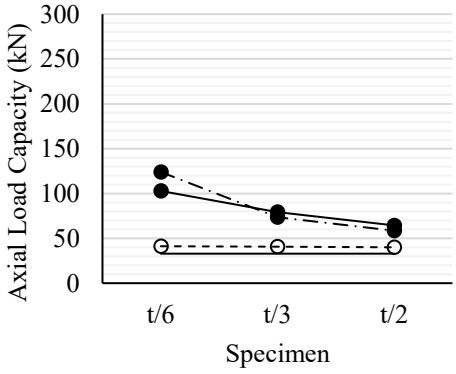

(e) kh/t = 31

Figure 6.3. Axial load capacity vs. eccentricity.

Chapter 7 Summary and Conclusions

7.1 Summary

This research aimed to study the behaviour of reinforced concrete masonry columns subjected to a combination of axial load and bending moment. Both experimental and numerical work were involved in this study. The experimental work involved testing of six concrete masonry columns of varying height incorporating design parameters of cross-sectional configuration, masonry compressive strength, axial load eccentricity, and axial load end eccentricity ratio. The numerical work consisted of development of a finite element model using SAP2000, and a parametric study of 20 archetype models on the effects of slenderness and load eccentricity. The behaviour and capacity of both physical specimens and FE models were presented and discussed in terms of load vs. deflection and moment-curvature relationships. The results were also compared with design values obtained using the Canadian and American Masonry Design Standard (CSA S304, TMS402/602) as appropriate.

7.2 Conclusion

Conclusions drawn from the results of this study are presented in the following.

Experimental program

The failure modes of specimens were dependent on their slenderness and loading conditions. At a low slenderness and under a concentric axial load, the failure was characterized by splitting longitudinal cracks and or localized crushing leading to buckling of longitudinal reinforcement. At a relatively high slenderness and under an eccentric axial

load, the failure was characterized by flexural tensile cracking and compressive crushing concentrating around the midspan of the specimens. Buckling of longitudinal reinforcement on the compression side of the specimens was also observed.

As the slenderness increased, the capacity of specimens decreased with increasingly pronounced nonlinearity at the outset of the loading. The failure was increasingly ductile and the specimen at failure exhibited significant mid-span deflection.

The comparison with the code values showed that while CSA S304 underestimates P_{ult} by an average of 30.6 percent, the TMS 402/602 P_{ult} values were much closer to the test results, especially for eccentrically loaded columns.

The comparison of experimental EI_{eff} values with the codes showed that CSA S304 underestimated EI_{eff} by 15% which results in overly conservative design. However, TMS 402/602 overestimated EI_{eff} by 90%. The difference in between the two codes is because unlike the CSA S304, the TMS 402/602 considers presence of axial load in calculation of cracked section moment of inertia.

While the TMS 402/602 overestimated EI_{eff} by 90%, it predicted P_{ult} values reasonably accurate. This suggests that calculating EI_{eff} of test specimens at one point along the column height to represent overall flexural rigidity of the column might be problematic.

Numerical program

The finite element model encoded in SAP2000 was shown to be capable of predicting the behaviour and capacity of masonry columns. The study of a wide range of slenderness

corroborated the findings from the experimental program. The axial load-bearing capability of reinforced concrete block masonry columns decreases as their effective slenderness increases. The rate of this decease is associated with the applied load eccentricity. As eccentricity increases, the decrease due to an increase in slenderness is not as pronounced as in the low eccentricity case.

Overall, CSA S304 tends to underestimate the capacity. However, for low slenderness and high eccentricity, CSA S304 performed reasonably well. For specimens with an effective slenderness greater than 30, the FE axial load capacity was significantly greater than that specified by of CSA S304. This discrepancy underscores CSA S304's restricted clause in placing an arbitrary limit in axial load on reinforced concrete masonry columns of high slenderness. On the other hand, TMS 402/602 provides more accurate predictions than CSA S304 for all slenderness and eccentricity ratios studied.

7.3 Recommendations for Future Research

Based on the experiences gathered through doing this research project and based on the conclusions, the following is recommended for future research:

1. **Extended Experimental Testing:** There is a need for extended experimental testing covering a broader range of masonry column specimens. Especially, focusing on those with extreme slenderness and varied eccentricities can provide a more holistic understanding of masonry column behavior.

2. **In-depth Analysis of Moment Magnification Factors:** The discrepancies between the codes and experimental results, particularly for the moment

magnification factor, suggest a focused study to establish more accurate predictive models.

3. **Comprehensive Parametric Studies:** The parameters covered in this research can be further diversified. For instance, considering different cross-sectional shapes, varying reinforcement configurations, and the inclusion of other external factors such as boundary conditions.

References

Design of Masonry Structures (CSA S304-14). 2019 ed. Mississauga(Ontario): Canadian Standards Association.

ASTM A1064/A1064M, 2013. *Standard Specification for Steel Wire and Welded Wire Reinforcement, Plain and Deformed, for Concrete.*

ASTM C140/C140M, 2023. *Standard Test Methods for Sampling and Testing Concrete Masonry Units and Related Units.* ASTM International (ASTM).

ASTM C270, 2019. *Standard Specification for Mortar for Unit Masonry.* ASTM.

CSA Group, 2014. *CAN/CSA-A179-14 Mortar and Grout for Unit Masonry.*

Drysdale, R. & Hamid, A., 2005. *Masonry Structures Behaviour and Design - Canadian Edition.* Mississauga(Ontario): Canada Masonry Design Centre.

Edgell, G. & Templeton, W., 1985. *Reinforced Brickwork Columns.* Melbourne, Australia, pp. 20-1, 20-16.

Euler, L., 1759. Sur la force des colonnes. *Memoires de l'Academie des Sciences de Berlin,* pp. 252-282.

Fattal, S. G. & Cattaneo, L. E., 1976. *Structural Performance of Masonry Walls Under Compression and Flexure,* US Department of Commerce, National Bureau of Standards.

Hasan, S. S. & Hendry, A. W., 1976. *The Effect of Slenderness and Eccentricity on the Compressive Strength of Walls.* Brugge, Fourth International Brick-Masonry Conference.

Hatzinikolas, M., Warwaruk, J. & Longworth, J., 1978. *Concrete Masonry Walls,* University of Alberta, Department of Civil Engineering.

Isfeld, A., Muller, A., Hagel, M. & Shrive, N., 2019. Analysis of Safety of Slender Concrete Masonry Walls in Relation to CSA S304-14. *Canadian Journal of Civil Engineering,* 46(5), p.04020072.

Khorramian, K., Sadeghian P., 2020. Experimental Investigation of Short and Slender Rectangular Concrete Columns Reinforced with GFRP Bars under Eccentric Axial Loads. *Journal of Composites for Construction*, 24(6), pp.

Liu, Y., 2002. *Beam-Column Behaviour of Masonry Structural Elements.* University of New Brunswick.

Liu, Y. & Dawe, J. L., 2003. Analytical Modeling of Masonry Load-Bearing Walls. *Canadian Journal of Civil Engineering,* 30(5), pp. 795-806.

Liu, Y. & Hu, K., 2007. Experimental Study of Reinforced Masonry Walls Subjected to Combined Axial Load and Out-of-Plane Bending. *Canadian journal of Civil Engineering,* 34(11), pp. 1486-1494.

Maksoud, A. A. & Drysdale, R. G., 1993. *Rational Moment Magnification Factor for Slender Unreinforced Masonry Walls.*, 6th North Amewrican Masonry Conference.

Ojinaga, J. & Turkstra, C. J., 1982. Design of Reinforced Masonry Walls and Columns for Gravity Loads. *Canadian Journal of Civil Engineering,* 9(1), pp. 84-95.

Popehn, J. R. B. et al., 2008. Influence of Transverse Loading on The Stability of Slender Unreinforced Masonry Walls. *Engineering Structures,* 30(10), pp. 2830-2839.

Priestley, M. J. N. & Elder, D., 1983. Stress-Strain Curves for Unconfined and Confined Concrete Masonry. *ACI Journal Preceedings,* 80(3), pp. 192-201.

Sturgeon, G., Longworth, J. & Warwaruk, J., 1971. *An Investigation of Reinforced Concrete Block Masonry Columns.* Edmonton(Alberta): University of Alberta Deprtment of Civil Engineering.

TMS 402/602-16, 2016. *Building Code Requirements and Specifications for Masonry Structures.* The Masonry Society.

Yokel, F. & Dikkers, R. D., 1971. Strength of Load Bearing Masonry Walls. *Journal of The Structual Division,* 97(5), pp. 1593-1609.

Yokel, F. Y., Mathey, R. G. & Dikkers, R. D., 1970. *Compressive Strength of Slender Masonry Walls,* Department of Commerce, National Bureau of Standards.

Appendix A: Auxiliary Tests and Results

Auxiliary tests were conducted to find physical and mechanical properties of mortar, grout, reinforcement, blocks, and prisms.

A.1 Concrete Masonry Units (CMUs)

Physical properties and compressive strength of the concrete masonry units (CMUs) were determined in accordance with requirements of the Standard Test Methods for Sampling and Testing Concrete Masonry Units and Related Units (ASTM C140/C140M). 6 random boundry and stretcher element units were each selected and tested under compression at Dalhousie University's Heavy Structures Laboraty using the Instron Universal Testing Machine. A typical testing setup is shown in Figure 7.1.

(a) Boundry element unit (b) Stretcher unit

Figure 7.1. Concrete masonry units typical testing configuration.

Dimensional properties of both boundary and stretcher units were measured using a digital caliper and averaged across all specimens as shown in Figure 7.2.

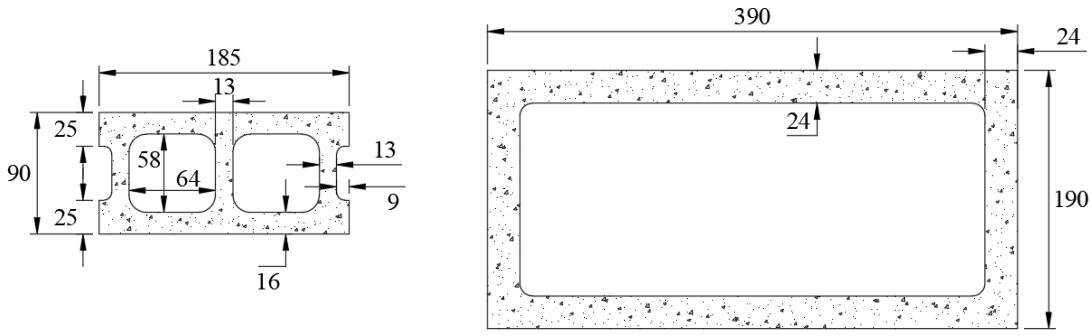

(a) Stretcher unit (b) Boundry element unit

Figure 7.2. Concrete masonry units dimensions.

The net cross-sectional area of stretcher and boundary units were measured as 8,923 mm^2 and 25,627 mm^2 respectively. Table 7.1 displays the compressive strength calculations for both stretcher and boundary units. Figure 7.3 displays typical failures of these blocks.

Table 7.1. Mechanical properties of CMUs

CMU type	Specimen ID	Ultimate Load (kN)	Ultimate Strength (MPa)	Average Compressive Strength (MPa)	COV Compressive Strength
Stretcher Unit	S1	206.4	23.1	25.6	10.0%
	S2	255.8	28.7		
	S3	224.3	25.1		
	S4	258.2	28.9		
	S5	215.7	24.2		
	S6	211.3	23.7		
	C1	831.9	32.5	35.8	10.9%

CMU type	Specimen ID	Ultimate Load (kN)	Ultimate Strength (MPa)	Average Compressive Strength (MPa)	COV Compressive Strength
Boundary Unit	C2	877.9	34.3		
	C3	926.0	36.1		
	C4	1109.0	43.3		
	C5	854.7	33.4		
	C6	902.8	35.2		

(a) Boundry element unit (b) Stretcher unit

Figure 7.3. Concrete masonry units typical failure patterns.

A.2 Mortar

Physical properties and compressive strength of the mortar samples were determined in accordance with requirements of the Standard Specification for Mortar for Unit Masonry (ASTM C270). 6 random samples from different batches were molded and cured in the moist room and tested under compression. A typical testing setup is shown in Figure 7.4. Mix design of the mortar is a proportion specified type S mortar based on Table 4 in CSA A179-14. This table provides volumetric proportions and the values presented in the following are converted weight ratios based on Shaw Resources Plant material densities.

- 5.5% Portland Cement
- 13.75% Type N
- 80.75% Sand

Water will be added until proper workability is reached.

Figure 7.4. A typical testing configuration of mortar specimens.

Table 7.2 displays the compressive strength of mortar samples and Figure 7.5 shows a typical failure of mortar specimens.

Table 7.2. Mechanical properties of mortar specimens.

Specimen Number	Ultimate Strength (MPa)	Average Compressive Strength (MPa)	COV Compressive Strength
1	9.0	11.7	14.2%
2	12.3		
3	14.6		
4	12.1		
5	11.3		
6	11.2		

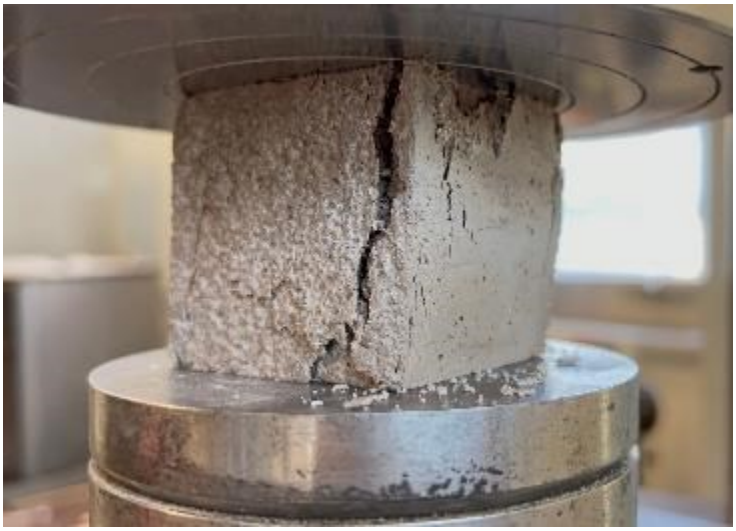

Figure 7.5. Mortar specimen typical failure.

A.3 Grout

Physical properties and compressive strength of the grout samples were determined in accordance with requirements of the Annex B of the CSA S304 code. 12 random samples from different batches were molded and cured in the moist room and tested under compression. A typical testing setup is shown in Figure 7.6. Mix design of the grout is based on Table 5 in CSA A179-14. This table provides volumetric proportions and the values presented in the following are converted weight ratios based on Shaw Resources Plant material densities.

- 25% Portland Cement
- 75% Sand

Water will be added until desires slump is reached.

Figure 7.6. Grout specimen typical testing configuration.

Table 7.3 displays the compressive strength of grout samples and Figure A.7 shows a typical failure of grout specimens.

Table 7.3. Mechanical properties of grout specimens

Specimen Number	Respective Column Specimen	Ultimate Strength (MPa)	Average Compressive Strength (MPa)	COV Compressive Strength
1	SS	28.9		
2	SS	27.4	26.8	2.2%
3	SS	26.2		
4	SC	20.1		
5	SC	22.4	22.0	6.3%
6	SC	23.4		
7	MS, TS	15.1		
8	MS, TS	13.3	13.9	5.9%
9	MS, TS	13.4		
10	MC, TC	23.4		
11	MC, TC	23.7	23.4	1.1%
12	MC, TC	23.1		

Figure A.7. A typical failure of grout specimens.

A.4 Prism

Prisms were constructed and tested in accordance with requirements of CSA S304. A total number of 27 prisms were constructed and tests. 6 prisms were built per each column with stretcher units and 3 prisms were built per each column with boundary element units. As shown in Figure 7.8 Prisms were built in stack pattern and 3 courses height without reinforcement. Prisms were cured in the same conditions as columns after construction and

tested under pure axial compression using the Instron Universal Machine. Prisms were capped using high density fibre boards.

(a) Stretcher prism (b) Boundry element prism

Figure 7.8. Typical prism specimens configuration and testing setup

Net cross-sectional area of masonry prisms was calculated as 74,100 mm^2 and 15,948 mm^2 for boundary element and stretcher masonry prisms respectively. Results of the prism compressive tests are presented in Table 7.4 and typical prism failure patterns are presented in Figure 7.9. Figure 7.10 shows stress-strain relationship of specimen TS1 during test. Elastic stiffness of prisms was calculated as slope of the stress-strain curve's initial linear part.

Table 7.4. Mechanical properties of prism specimens

Specimen Type	Specimen ID	Compressive Strength			Elastic Stiffness		
		Ultimate Strength (MPa)	Average (MPa)	CV	Elastic Stiffness (MPa)	Average (MPa)	COV
Boundary Element	SC1	15.7	18.5	16.9%	13,157	15,856	19.5%
	SC2	22.9			20,173		
	SC3	17.0			14,240		
	MC1	20.2	20.5	10.4%	15,681	17,061	8.3%
	MC2	18.1			16,503		
	MC3	23.3			19,000		
	TC1	19.8	19.3	2.2%	15,265	15,547	4.0%
	TC2	19.1			14,974		
	TC3	18.8			16,404		
Stretcher Element	SS1	8.6	8.5	17.3%	7,401	7,482	22.1%
	SS2	7.4			5,887		
	SS3	11.6			11,004		
	SS4	8.2			7,042		
	SS5	7.8			7,129		
	SS6	7.3			6,430		
	MS1	8.0	7.9	16.5%	8,366	7,896	16.0%
	MS2	7.2			7,978		
	MS3	7.0			6,732		
	MS4	6.9			6,681		
	MS5	7.7			7,244		
	MS6	10.7			10,375		
	TS1	11.5	9.5	15.9%	11,269	9,307	15.9%
	TS2	8.6			8,370		
	TS3	7.1			6,954		

Specimen Type	Specimen ID	Compressive Strength			Elastic Stiffness		
		Ultimate Strength (MPa)	Average (MPa)	CV	Elastic Stiffness (MPa)	Average (MPa)	COV
	TS4	10.7			10,497		
	TS5	8.7			8,529		
	TS6	10.5			10,220		

(a) Stretcher prism (b) Boundry element prism

Figure 7.9. A Typical failure of prism specimens.

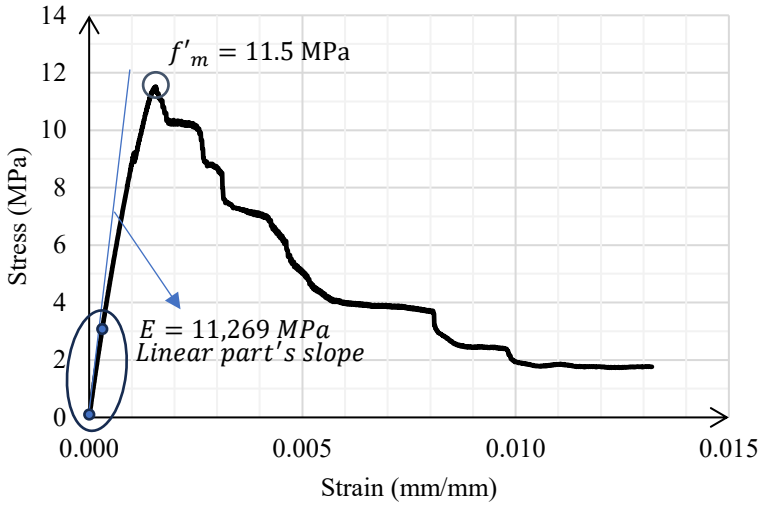

Figure 7.10. Prism stress-strain relationship (specimen TS1).

A.5 Reinforcement

Physical properties and tensile strength of the reinforcement steel bar samples were determined in accordance with requirements of the Standard Specification for Steel Wire and Welded Wire Reinforcement, Plain and Deformed, for Concrete (ASTM A1064/A1064M). 5 random samples were cut installed under tention. A typical testing setup is shown in Figure 7.11.

Figure 7.11. Reinforcement steel rebar specimen typical testing configuration.

Table 7.5 displays the mechanical properties of rebar samples and Figure 7.12 shows a typical failure of rebar specimen.

Table 7.5. Mechanical properties of reinforcement speciments

Specimen Number	Yield Strength, F_y (MPa)	Average Yield Strength (MPa)	CV Tensile Strength	E_s (MPa)	Ultimate Strength, F_t (MPa)	Average Ultimate Strength (MPa)	COV Ultimate Strength
1	370				564		
2	375				565		
3	398	381	3.0%	201,261	589	571	2.1%
4	371				560		
5	391				580		

Figure 7.12. Typical reinforcement steel rebar specimen failure

Appendix B: Sample Calculations Based on CSA S304 and TMS 402/602 Codes

In this appendix, sample calculations for specimen TS based on CSA S304 and TMS 402 is presented.

Specimen TS had a height of 3050 mm and its cross-sectional dimensions are presented in Figure 7.1. specified compressive strength, f'_m of specimen TS is 9.5 MPa and the yield strength of the longitudinal rebars, F_y is 381 MPa based on auxiliary test results.

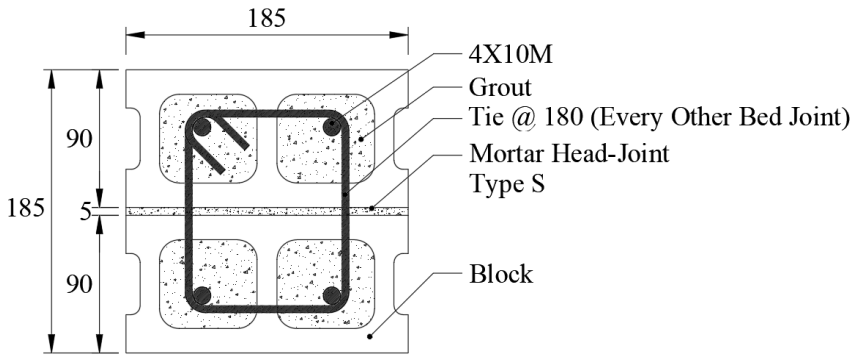

Figure 7.1. Specimen TS cross-sectional propoerties.

CSA S304 Sample Calculations:

Based on CSA S304, calculation of EI_{eff} and magnified moment for this specimen under eccentricity of 63.3 mm is as follows. Column's axial capacity in accordance with the CSA S304 at e = 63.3 mm (P = 99 kN) is used for this example.

General material mechanical properties and section properties are calculated as follows:

$A_e = 185 \times 185 \rightarrow A_e = 34{,}225\ mm^2$

$$S_e = \frac{185 \times 185^2}{6} \rightarrow S_e = 1{,}055{,}271\ mm^3$$

$$e_k = \frac{S_e}{A_e} = \frac{1{,}055{,}271}{34{,}225} \rightarrow e_k = 30.8\ mm$$

$$d = 135\ mm$$

$$d' = 50\ mm$$

$E_m = 9{,}307\ MPa$ (based on test results)

$$n = \frac{E_s}{E_m} = \frac{201{,}261}{9307} \rightarrow n = 21.6$$

$$I_o = \frac{ba^3}{12} + (n-1)A_s'\left(d' - \frac{t}{2}\right)^2 + (n-1)A_s\left(d - \frac{t}{2}\right)^2$$

$$= \frac{185 \times 185^3}{12} + (21.6-1) \times 200 \times \left(50 - \frac{185}{2}\right)^2$$

$$+ (21.6-1) \times 200 \times \left(135 - \frac{185}{2}\right)^2 \rightarrow I_o = 1.12 \times 10^8\ mm^4$$

$$kd = \sqrt{\left(\sum_{i=1}^{2} \frac{nA_{s_i}}{b}\right)^2 + 2\sum_{i=1}^{2} \frac{nA_{s_i}d_i}{b}} - \sum_{i=1}^{2} \frac{nA_{s_i}}{b} = \sqrt{(46.5)^2 + 2 \times 4{,}298} - 46.5 \rightarrow kd$$

$$= 57.2\ mm$$

Cracked section's moment of inertia based on CSA S304 is calculated below.

$$I_{cr} = \frac{b(kd)^3}{3} + \sum_{i=1}^{2} bA_{s_i}(d_i - kd)^2 \rightarrow I_{cr} = 3.78 \times 10^7\ mm^4$$

Effective flexural rigidity (EI_{eff}) is calculated below.

$$(EI)_{eff} = E_m\left[0.25I_o - (0.25I_o - I_{cr})\left(\frac{e - e_k}{2e_k}\right)\right]$$

$$= 9{,}307\left[0.25 \times 1.12 \times 10^8\right.$$

$$\left. - (0.25 \times 1.12 \times 10^8 - 3.78 \times 10^7)\left(\frac{63.3 - 30.8}{2 \times 30.8}\right)\right] \rightarrow (EI)_{eff}$$

$$= 3.09 \times 10^{11}\ N.mm^2$$

Cracking flexural rigidity EI_{cr} is

$$EI_{cr} = E_m I_{cr} = 9{,}307 \times 3.78 \times 10^7 \rightarrow (EI)_{eff,min} = 3.52 \times 10^{11}\ N.mm^2$$

Maximum permissible EI is

$$(EI)_{eff,max} = 0.25E_m I_o = 0.25 \times 9{,}307 \times 1.12 \times 10^8 \rightarrow (EI)_{eff,max}$$

$$= 2.62 \times 10^{11}\ N.mm^2$$

As calculated EI_{eff} is lower than EI_{cr}, the value of EI_{cr} is used as the final EI_{eff}.

$$EI_{eff} = EI_{cr} = 3.52 \times 10^{11} N.mm^2$$

Euler buckling load according to CSA S304 at P = 147 kN is

$$P_{cr} = \frac{\pi^2 \phi_{er}(EI)_{eff}}{[1 + 0.5\beta_d](kh^2)} = \frac{\pi^2 \times 1 \times 3.52 \times 10^{11}}{[1 + 0.5 \times 1](1 \times 3050^2)} \rightarrow P_{cr} = 248.7\ kN$$

Magnification factor in accordance with the CSA S304 is calculated below.

$$\delta = \frac{C_m}{\left(1 - \frac{P_f}{P_{cr}}\right)} = \frac{1}{\left(1 - \frac{99}{248.7}\right)} \rightarrow \delta = 1.66$$

Finally, the magnified moment at P = 99 kN is

$$M_{f,tot} = \delta M_f = 1.66 \times \left(99 \times \left(\frac{63.3}{1000}\right)\right) \rightarrow M_{f,tot} = 10.4\ kN.m$$

TMS 402/602 Sample Calculations:

Based on TMS 402/602, calculation of EI_{eff} and magnified moment for this specimen under eccentricity of 63.3 mm is as follows. Column's axial capacity in accordance with the TMS 402/602 at e = 63.3 mm (P = 133 kN) is used for this example.

Cracking moment for P_u = 133 kN is

$$M_{cr} = \left(f_r + \frac{P}{A_g}\right)S = \left(1 + \frac{133 \times 10^3}{185 \times 185}\right)\left(\frac{185 \times 185^2}{6}\right) \rightarrow M_{cr} = 5.2\ kN.m$$

As $M_u = 8.4\ kN.m$ is higher than the cracking moment, based on the TMS 402/602, I_{eff} shall be taken as I_{cr} calculated as follows.

$$I_{cr} = n\left(A_s + \frac{P_u}{f_y}\frac{t_{sp}}{2d}\right)(d-c)^2 + \frac{bc^3}{3}$$

$$= 21.6\left(200 + \frac{133 \times 10^3}{381}\frac{185}{2 \times 135}\right)(135-101)^2 + \frac{185 \times 101^3}{3} \rightarrow I_{cr}$$

$$= 7.42 \times 10^7\ mm^4$$

where c is calculated as follows.

$$P_u = 0.8f'_m(0.8c)b + A'_sE_s\frac{c-d'}{d}0.003 - A_sE_s\frac{d-c}{c}0.003$$

$$133{,}000 = 0.8 \times 9.5 \times 0.8c \times 185 + 200 \times 201{,}261 \times \frac{c-50}{c} \times 0.003$$

$$- 200 \times 201{,}261 \times \frac{135-c}{c} \times 0.003 \rightarrow c = 101\ mm$$

$$EI_{eff} = E_m I_{cr} = 9{,}307 \times (7.42 \times 10^7) \rightarrow EI_{eff} = 6.91 \times 10^{11}\ N.mm^2$$

Euler buckling load and moment magnification factor based on the TMS 402/602 code is calculated as follows:

$$P_e = \frac{\pi^2 E_m I_{eff}}{h^2} = \frac{\pi^2 \times 6.91 \times 10^{11}}{3050^2} \rightarrow P_e = 732.7\ kN$$

$$\psi = \frac{1}{1 - \frac{P_u}{P_e}} = \frac{1}{1 - \frac{133}{732.7}} \rightarrow \psi = 1.22$$

Magnified moment is calculated as follows.

$$M_u = \psi M_{u,o} = 1.22 \times \left(133 \times \frac{63.3}{1000}\right) \rightarrow M_c = 10.3\ kN.m$$